Published in final edited form as:

Cancer Discov. 2023 December 12; 13(12): 2632–2651. doi:10.1158/2159-8290.CD-23-0601.

p53 gain-of-function mutation induces metastasis via Brd4-dependent Csf-1 expression

Gizem Efe[1,2], **Karen J. Dunbar**[1], **Kensuke Sugiura**[1], **Katherine Cunningham**[1], **Saul Carcamo**[3], **Spyros Karaiskos**[1], **Qiaosi Tang**[1], **Ricardo Cruz-Acuña**[1], **Lois Resnick-Silverman**[4], **Jessica Peura**[5], **Chao Lu**[1,2], **Dan Hasson**[3,4,6], **Andres J. Klein-Szanto**[7], **Alison M. Taylor**[1,8], **James J. Manfredi**[4], **Carol Prives**[1,9], **Anil K. Rustgi**[1,10,*]

[1]Herbert Irving Comprehensive Cancer Center, Columbia University, New York, NY, 10032, USA.

[2]Department of Genetics and Development, Columbia University, New York, NY, 10032, USA.

[3]Tisch Cancer Institute Bioinformatics for Next Generation Sequencing (BiNGS) core, Icahn School of Medicine at Mount Sinai, New York, NY, 10029, USA.

[4]Department of Oncological Sciences, Icahn School of Medicine at Mount Sinai, New York, NY, 10029, USA.

[5]Division of Hematology-Oncology, University of Massachusetts Medical School, Worcester, MA, 01655, USA.

[6]Graduate School of Biomedical Sciences, Icahn School of Medicine at Mount Sinai, New York, NY, 10029, USA.

[7]Histopathology Facility, Fox Chase Cancer Center, Philadelphia, PA, 19111, USA.

[8]Department of Pathology and Cell Biology, Columbia University, New York, NY, 10032, USA.

[9]Department of Biological Sciences, Columbia University, Columbia University, New York, NY, 10032, USA.

[10]Division of Digestive and Liver Diseases, Department of Medicine, Columbia University, New York, NY, 10032, USA.

Abstract

TP53 mutations are frequent in esophageal squamous cell carcinoma (ESCC) and other SCCs, and are associated with a proclivity for metastasis. Here, we report that Colony-stimulating factor-1 (Csf-1) expression is upregulated significantly in a p53-R172H-dependent manner in metastatic lung lesions of ESCC. The p53-R172H-dependent Csf-1 signaling through its cognate receptor

[*]**Address Correspondence to:** Anil K. Rustgi, MD, Herbert and Florence Irving Professor of Medicine, Herbert Irving Comprehensive Cancer Center, Columbia University Irving Medical Center, 1130 St. Nicholas Ave, ICRC 2-201, New York, NY 10032, USA. Phone: (212) 305-0983, akr2164@cumc.columbia.edu.

Author contributions

G.E., K.J.D. and K.C. performed experiments and data analysis. K.S., Q.T, R.C.A, L.R.-S. and J.P. assisted with experiments. A.J.K.-S. performed pathology scoring. S.C. and S.K. performed CUT&RUN-seq and RNA-seq analysis. C.L., D.H., A.M.T., J.J.M. and C.L.P. designed the experiments and reviewed the manuscript. A.K.R. designed the experiments, performed data analysis, and wrote the manuscript. G.E. also wrote the manuscript.

The authors declare no competing interests.

Csf-1r increases tumor cell invasion and lung metastasis, which in turn is mediated in part through Stat3 phosphorylation and epithelial-to-mesenchymal transition. In *Trp53*^{R172H} tumor cells, p53 occupies the *Csf-1* promoter. The *Csf-1* locus is enriched with histone 3 lysine 27 acetylation (H3K27ac), which likely is permissive for fostering an interaction between Brd4 and p53-R172H to regulate *Csf-1* transcription. Inhibition of Brd4 not only reduces tumor invasion and lung metastasis, but also reduces circulating Csf-1 levels. Overall, our results establish a novel p53-R172H-dependent Brd4-Csf-1 axis that promotes ESCC lung metastasis, and suggest avenues for therapeutic strategies for this difficult-to-treat disease.

Keywords

p53 mutations; CSF-1/CSF-1R signaling; BRD4; tumor invasion; lung metastasis

Introduction

Tumor metastasis is a major barrier to effective cancer therapy, and metastasis is associated with more than 90% of cancer-related mortality [1, 2]. Both intrinsic factors, including genomic instability and epigenetic alterations, and extrinsic factors, such as microenvironmental cues, have been implicated in the metastatic proclivity of cancer cells [3]. The precise biological mechanisms underlying metastasis, however, require more extensive elucidation in order to improve the potential for novel therapeutics.

TP53 (*Trp53* in mice) that encodes the p53 protein is mutated frequently in human cancers, and *TP53* mutations correlate with higher metastatic rates and poor patient survival [4]. Approximately 70% of *TP53* mutations are missense, resulting in loss of wild-type p53 tumor suppressor activity and/or acquisition of dominant negative (DN) functions [5, 6]. Additionally, some missense mutations may result in gain-of-function (GOF) properties that are pro-tumorigenic as a result of DNA binding, interactions with other transcription factors and chromatin modifiers or modulation of p63, an ortholog of p53 [7–11]. The most frequent "hotspot" *TP53* missense mutations cluster within the p53 DNA-binding domain and include codons 175 (codon 172 in mice, which is the focus of this study), 245, 248, 249, 273 and 282 [12]. These hotspot p53 mutations have been reported to have different roles in promoting cancer cell proliferation, survival, migration, invasion, epithelial-to-mesenchymal transition (EMT), angiogenesis and metastasis [4, 13–15]. However, it is not clear how these mutations foster metastasis, catalyzing our desire to elucidate the underlying mechanisms.

Esophageal cancer is highly aggressive and is the sixth leading cause of cancer-related mortality worldwide. It is projected that there will be 957,000 new esophageal cancer cases worldwide by 2040 [16]. Esophageal cancer comprises two predominant subtypes, esophageal squamous cell carcinoma (ESCC) and esophageal adenocarcinoma (EAC), with ESCC being more prevalent globally [17, 18]. Most patients with ESCC or EAC present with metastases, primarily to the lungs [18]. *TP53* mutations are found in approximately 80% of ESCC cases, with the majority of mutations located in the DNA-binding domain [19, 20].

How p53 mutations can modulate growth factors, cytokines and chemokines to foster ESCC metastasis require elucidation. Our novel study establishes Colony Stimulating Factor-1 (Csf-1) as one of the secreted cytokines that potentiates ESCC tumor cell invasion and lung metastasis in a *Trp53*^{R172H}-dependent manner. Canonically, CSF-1 recruits M2-like tumor-associated macrophages (TAMs) and CD11b^{+}Gr-1^{Low}Ly6C^{High} myeloid-derived suppressor cells (MDSCs) by binding to its tyrosine kinase receptor Colony Stimulating Factor-1 Receptor (CSF-1R) [21, 22]. While it has not been studied extensively, CSF-1R can be expressed on epithelial cells, regulating downstream pathways involved in proliferation, differentiation, and metastasis [23, 24].

We have demonstrated that p53-R172H occupies the *Csf-1* promoter and regulates its transcription. The *Csf-1* gene locus contains high levels of H3K27ac, a promoter and enhancer marker that is indicative of active transcription [25, 26]. The epigenetic reader BRomodomain-containing Domain 4 (BRD4), a member of the Bromodomain and Extraterminal (BET) protein family, binds to acetylated lysine residues at the promoter and super-enhancers, leading to the assembly of the transcription complex and the transcription initiation of oncogenes such as *c-Myc* and *Fosl* [27]. Therefore, we hypothesized that Brd4 might interact with p53-R172H to induce *Csf-1* expression. We have used genetic deletion and complementary pharmacological inhibition studies to demonstrate that loss of Csf-1 or Brd4 significantly reduces tumor cell invasion and lung metastasis through regulation of Stat3 activation and EMT in lung metastasis in a p53-R172H-dependent manner. Therefore, we advocate targeting the CSF-1/CSF-1R axis in patients with metastatic ESCC, an area bereft of impactful therapeutics. Given the common genomic properties of ESCC, head/neck SCC and lung SCC [28–31] our nomination of the CSF-1/CSF-1R axis may be applicable to therapeutic approaches for other SCCs.

Results

p53-R172H binds to the promoter of *Csf-1* and fosters its expression in metastatic ESCC

We generated a 4-Nitroquinoline N-oxide (4-NQO) and *Trp53*^{R172H}-driven ESCC mouse model and derived cell lines from esophageal tumors of *Trp53*$^{+/+}$, *Trp53*$^{-/-}$, and *Trp53*$^{R172H/-}$ mice after 4-Nitroqinoline 1-oxide (4-NQO) administration in drinking water [32]. 4-NQO is a water-soluble quinoline derivative that causes DNA adduct formation and production of reactive oxygen species (ROS), resulting in oral-esophageal squamous cell carcinoma in mice [33]. To better understand potential mediators of p53-R172H-driven metastasis, we performed bulk RNA-seq of metastatic ESCC cells to the lungs with Trp*53*$^{R172H/-}$ (control) or *Trp53*^{R172H}-depletion (shCtrl-M and shTrp53-M, respectively). We verified p53 protein levels in the different experimental conditions (Supplementary Fig. S1a) [34].

From the RNA-seq data, we found 260 upregulated genes and 291 downregulated genes in shCtrl-M compared with shTrp53-M (P_{adj}<0.05 and |$\log_2$ fold change|>2) (Fig. 1a). As expected, *Trp53* was amongst the most differentially expressed genes, which served as an internal control (Figs. 1a and 1b). *Csf-1* was upregulated (~2.8-fold) in shCtrl-M cells compared to shTrp53-M cells and was amongst the most upregulated genes, including the metallopeptidase inhibitor *Timp1* that has been demonstrated previously to contribute to

metastasis through senescence reprogramming [35] (Figs. 1a, 1b and Supplementary Fig. S1b). Furthermore, we have identified genes that are downregulated in the primary and metastatic tumors (shCtrl and shTrp53), such as tight junction protein *MAL and relevant proteins for vesicle trafficking and membrane link domain 3* (*Marveld3*). This gene has been demonstrated to reduce cell migration, EMT and metastasis in non-small cell lung cancer (NSCLC) through the suppression of the Wnt/β-catenin signaling pathway [36] (Supplementary Fig. S1c).

In a complementary approach, we conducted a cytokine array analysis on conditioned media from shCtrl-M (n=5 cell lines) and shTrp53-M cells (n=3 cell lines). Amongst the 62 cytokines examined, we identified FAS ligand, Fractalkine (Cx3cl1), interleukin 6 (IL-6), IL-9, IL-10 and Csf-1 with higher secretion from control cells, suggesting their potential involvement in $Trp53^{R172H}$-dependent metastasis (Fig. 1c). Of these six cytokines, Csf-1 and Fractalkine were secreted at the highest concentrations, but as mentioned, only *Csf-1* was amongst the top upregulated genes. We assessed Csf-1 secretion by enzyme-linked immunosorbent assay (ELISA) and found that metastatic tumor cells with $Trp53^{R172H/-}$ secreted more Csf-1 than those with $Trp53^{R172H/-}$ depletion (Fig. 1d). Additionally, primary ESCC cells with $Trp53^{R172H/-}$ secreted higher Csf-1 levels compared to either $Trp53^{-/-}$ or $Trp53^{+/+}$ cells (Fig. 1e).

To elucidate the relationship between p53-R172H and *Csf-1*, we conducted ChIP-qPCR for p53 in five $Trp53^{R172H/-}$ metastatic ESCC cell lines and found that the *Csf-1* promoter region was highly enriched with p53-R172H occupancy, suggesting that *Csf-1* is a gene target of p53-R172H (Fig. 1f). These data indicate that p53-R172H regulates *Csf-1* transcription and suggest that Csf-1 may be a potential mediator of $Trp53^{R172H/-}$-dependent ESCC metastasis.

The Csf-1/Csf-1r signaling axis fosters ESCC lung metastasis

To study the functional role of the Csf-1/Csf-1r signaling in ESCC metastasis, we deleted *Csf-1* in mouse $Trp53^{R172H/-}$ tumor cells using a ribonucleoprotein (RNP)-based CRISPR/Cas9 approach (Supplementary Figs. S1d, S1e and Fig. 2a). We detected no changes in the expression of *IL-34*, which encodes the other ligand that binds Csf-1r, upon the deletion of *Csf-1* (Supplementary Fig. S1f) [37, 38]. Deletion of *Csf-1* in $Trp53^{R172H/-}$ tumor cells significantly reduced the number of invading tumor cells (Fig. 2b).

Next, we assessed the effects of Csf-1 on tumor progression in athymic nude mice ($CD1^{nu/nu}$) using the same cell lines described above. We first examined primary tumor growth following subcutaneous implantation and found that *Csf-1* deletion reduced tumor growth starting at Day 12 post-injection (Fig. 2c), resulting in a 2–3-fold decrease in tumor weight at the endpoint (Day 28) (Fig. 2d). We then stained the formalin fixed, paraffin-embedded (FFPE) tumor sections for Ki67 and found that the non-target controls had a higher percentage of $Ki67^{+}$ tumor cells than both *Csf-1* knockout clones (Fig. 2e). While these results are encouraging, it is possible that crosstalk might occur between flank tumors that can influence tumor progression [39].

To investigate the contribution of *Trp53*$^{R172H/-}$-dependent Csf-1 to ESCC metastasis, we conducted lateral tail-vein injections with 1.0×10^6 *Csf-1* KO or non-target control *Trp53*$^{R172H/-}$ tumor cells and assessed the tumor burden of lung metastases at the end of Week 8 (Fig. 2f). *Csf-1* deletion significantly reduced the metastatic tumor burden in the lungs (Fig. 2g). Provocatively, when Csf-1 was overexpressed in *Trp53*$^{-/-}$ and *Trp53*$^{+/+}$ cells (Supplementary Figs. S2a and S2b), there were no significant changes in the lung metastases as quantified by the number of YFP$^+$ metastatic foci and the percentage of mice with metastatic tumors after injection with these cells (Supplementary Figs. S2c and S2d). Upon repeating the lateral tail-vein injections with *shTrp53/Csf-1 KO* cells and *shTrp53/non-target controls* (Supplementary Fig. S2e), no difference was observed in the number of metastatic foci in the lungs (Fig. 2h). Overall, our data demonstrate that *Trp53*^{R172H}-dependent *Csf-1* upregulation has a functional role in tumor cell invasion and metastasis.

Csf-1/Csf-1r autocrine signaling promotes epithelial-to-mesenchymal transition

While it is known that CSF-1 mediates the crosstalk between tumor cells and macrophages [21, 22], the functional consequences of CSF-1/CSF-1R autocrine signaling have not been explored. We found that Csf-1r was expressed in metastatic and primary ESCC cells (Fig. 3a and Supplementary Fig. S2f), and to decipher its functional role, we treated *Trp53*$^{R172H/-}$, *Trp53*$^{-/-}$ or *Trp53*$^{+/+}$ primary tumor cells with a mouse Csf-1r (AFS98) monoclonal neutralizing antibody. This treatment reduced the number of invading *Trp53*$^{R172H/-}$ tumor cells, but it did not affect the invasive properties of *Trp53*$^{-/-}$ or *Trp53*$^{+/+}$ cells (Fig. 3b).

To delineate effectors of the Csf-1/Csf-1r signaling, we identified gene expression patterns that correlated with *CSF-1* expression in TCGA SCC cases (including lung SCC, head and neck SCC, esophageal SCC, cervical SCC and a subset of bladder cancers classified as basal squamous). Unbiased gene set enrichment analysis (GSEA) revealed that IL6/JAK/STAT3, Epithelial-to-Mesenchymal Transition (EMT) and angiogenesis correlate significantly with high *CSF-1* expression, and have been implicated in the mediation of tumor metastasis (Figs. 3c, and 3d, Supplementary Figs. S3a and S3b). The EMT pathway was also enriched in shCtrl-M compared to shTrp53-M as revealed in our RNA-seq data with the ESCC tumor cells harboring *Trp53*$^{R172/-}$ (Supplementary Fig. S3c).

To pursue the connection between Csf-1 signaling and Stat3, we examined the levels of total Stat3 and phosphorylated Stat3 (Tyr705), which are associated with activation of Stat3 signaling and EMT processes [40]. Phosphorylated Stat3 levels were higher in cells expressing p53-R172H than in those expressing wild-type p53 or lacking p53 (Figs. 3e and 3f). Upon Csf-1r inhibition, both total and phosphorylated Stat3 decreased only in p53-R172H cells, and phosphorylated Stat3 levels were reduced to the levels similar to those in p53 null or wild-type p53 cells (Figs. 3e – 3g). In addition, we evaluated the EMT pathway and discovered that treatment with Csf-1r neutralizing antibody downregulated *Twist1* and *Zeb1* in *Trp53*$^{R172H/-}$ cells, but not p53 null or wild-type p53 cells (Fig. 3h). Metastatic lung lesions with *Trp53*^{R172H} *Csf-1* KO #1 and KO #2 had a lower nuclear Stat3 H-score than lesions with intact Csf-1 (Fig. 3i). Upon Csf-1r neutralizing antibody treatment, the level of E-Cadherin (E-Cad) was elevated only in metastatic shCtrl-M cells with p53-R172H (Fig. 3j). Furthermore, the percentage of E-Cad^{High} cells was increased in the metastatic lung

lesions with *Trp53*$^{R172H/-}$ upon *Csf-1* deletion (Fig. 3k). Similarly, metastatic tumors with *Trp53*^{R172H} had a higher H-score for another epithelial marker pan-cytokeratin (pan-CK) when *Csf-1* was deleted (Supplementary Fig. S3d). Interestingly, in addition to E-Cad and pan-CK expression, *Trp53*$^{R172H/-}$ metastatic lung lesions with Csf-1 KO had lower elongated cell scores than the control lesions, indicating a more epithelial morphology upon deletion of *Csf-1* (Supplementary Fig. S3e). Overall, our results suggest that blocking the p53-R172H-dependent Csf-1/Csf-1r signaling axis maintains metastatic tumor cells in the epithelial state.

Brd4 is a co-regulator of p53-R172H-dependent *Csf-1* transcription

To elucidate the mechanism by which *Trp53*^{R172H} regulates *Csf-1* transcription, we conducted Cleavage Under Targets and Release Using Nuclease sequencing (CUT&RUN-seq) for histone 3 lysine 27 acetylation (H3K27ac), an active enhancer and promoter marker [41], in *Trp53*$^{R172H/-}$ and *Trp53*$^{+/+}$ ESCC cells. Principal component analysis (PCA) based upon H3K27ac profiles demonstrated that the ESCC cells with *Trp53*$^{R172H/-}$ separated distinctively from the *Trp53*$^{+/+}$ cells (Supplementary Fig. S3f). Genome-wide analysis revealed a total of 904 regions with enriched H3K27ac and 1255 regions with depleted H3K27ac in *Trp53*$^{R172H/-}$ tumor cells compared to *Trp53*$^{+/+}$ cells (P_{adj}<0.05; Supplementary Figs. S3g and S3h). Notably, H3K27ac was reduced across the *Cdh1* gene body encoding the E-Cad and were enriched across the *Vim* gene body encoding the Vimentin in *Trp53*$^{R172H/-}$ cells compared to *Trp53*$^{+/+}$ cells (Supplementary Fig. S3i). H3K27ac was enriched across the *Csf-1* locus including the promoter site in *Trp53*$^{R172H/-}$ ESCC cells compared to *Trp53*$^{+/+}$ cells (Fig. 4a), suggesting that the *Csf-1* locus is active in the presence of p53-R172H (Fig. 4a).

The epigenetic reader Brd4 binds to acetylated histone lysine residues at promoters and super-enhancers to regulate transcription initiation [27]. We therefore investigated whether Brd4 was recruited to enriched H3K27ac sites in ESCC cells to induce *Csf-1* transcription. We found that global Brd4 levels in *Trp53*$^{R172H/-}$ tumor cells were ~2-fold higher than those in *Trp53*$^{-/-}$ cells and ~3-fold higher than in *Trp53*$^{+/+}$ cells (Fig. 4b). To investigate the relationship between Brd4 and p53, we performed a Proximity Ligation Assay (PLA) in mouse *Trp53*$^{R172H/-}$, *Trp53*$^{+/+}$, and *Trp53*$^{-/-}$ ESCC cells and found a close proximity between Brd4 and p53-R172H, but not with wild-type p53 (Fig. 4c). To test whether these findings could be extended to human cells, we deleted endogenous *TP53*^{R110L} in TE11 esophageal cancer cells [42], and then ectopically expressed p53-R175H (Fig. 4d). We also deleted endogenous *TP53*^{R175H} in LS123 colorectal cancer cells [43] (Fig. 4e). Using these human cancer cell lines, we observed higher PLA signals in cells expressing BRD4 and p53-R175H than in cells lacking p53 or expressing p53-R110L (Fig. 4f).

Next, cells were treated with a Brd4 small molecular inhibitor, JQ1 [44] or a PROTAC, ZXH-3–26, which selectively binds Brd4 and Cereblon, the substrate adaptor of the Cul4A E3 ligase complex that results in Brd4 ubiquitination and subsequent proteasomal degradation [45]. In two separate *Trp53*$^{R172H/-}$ ESCC cell lines, the PLA signal virtually disappeared upon Brd4 degradation, indicating that Brd4 was required for the PLA signal (Fig. 4g, h). As a control, c-Myc that is known to be regulated by Brd4 [46], was

downregulated (Fig. 4g). No difference was detected with another BET protein, namely, Brd2 [47, 48] suggesting the specificity of ZXH-3–26 (Supplementary Fig. S4a). JQ1 or ZXH-3–26 treatment significantly reduced *Csf-1* expression (Fig. 4i) and secretion (Fig. 4j). These results indicated that Brd4 is a critical co-regulator of p53-R172H-dependent *Csf-1* expression.

Targeting Brd4 reduces ESCC lung metastasis

As a complementary approach, we utilized two shRNAs to deplete Brd4 and verified that they effectively knocked down Brd4 in two mouse *Trp53*$^{R172H/-}$ ESCC cell lines at both mRNA (Supplementary Fig. S4b) and protein (Fig. 5a) levels, while not affecting Brd2 (Supplementary Fig. S4c). Similar to ZXH-3–26 treatment of these cells, c-Myc was downregulated upon Brd4 depletion (Fig. 5a). *Trp53*$^{R172H/-}$ ESCC cells with *Brd4* knockdown secreted less Csf-1 (Fig. 5b) and had decreased invasion capability (Fig. 5c), which were recapitulated upon treating parental cells with pooled siRNAs targeting *Brd4* (Supplementary Figs. S4d - S4g).

To investigate the role of Brd4 in lung metastasis, we treated mice with JQ1 or the vehicle control every other day between Days 7 and Day 53 after tail-vein injection of *Trp53*$^{R172H/-}$ ESCC cells (Fig. 5d). We observed a dramatic decrease in lung metastasis upon JQ1 treatment (Fig. 5e). Mechanistically, JQ1 treatment decreased nuclear Stat3 in metastatic tumors, indicating reduced activation of the protein and supporting the notion that Brd4 and Csf-1 are in the same axis in regulating Stat3 (Fig. 5f), compared to the control group. It is noteworthy that E-Cad expression increased upon depletion of Brd4 in *Trp53*$^{R172/-}$ tumor cells (Fig. 5g) and the percentage of E-Cad^{High} cells increased in lung metastatic lesions upon treatment with JQ1 (Fig. 5h).

Furthermore, we collected blood sera from these experimental mice with lung metastasis at Day 56 to assess circulating Csf-1 levels. Interestingly, while control mice with metastatic tumors had elevated circulating Csf-1 levels (2800 pg/mL on average) compared to mice without any tumors, JQ1 treatment reduced the mean Csf-1 level to ~1800 pg/mL, which is approximately the level in mice without any tumors (Fig. 5i). These results provided an *in vivo* support for our hypothesis that Brd4 is an upstream regulator of Csf-1 expression in promoting *Trp53*^{R172H}-driven lung metastasis.

Csf-1/Csf-1r signaling constitutes a therapeutic vulnerability in ESCC

We next conducted an in-depth analysis of CSF-1, CSF-1R and p53 expression in human ESCC samples. Initially, we stained tissue microarrays (TMAs) containing 148 ESCC and 47 normal tissues for CSF-1, CSF-1R and p53. Both CSF-1 (Fig. 6a) and CSF-1R (Supplementary Fig. S5a) levels were significantly higher in tumors than in adjacent normal tissues. Moreover, ESCCs with higher p53 expression, in most cases indicating mutant p53 leading to more stable p53, whose accumulation is regarded as a hallmark of cancer cells [49], had significantly elevated CSF-1 expression (Fig. 6b).

We then interrogated the TCGA for squamous cell carcinomas (SCCs) as noted previously [30] since *TP53* mutations are the most frequently identified gene mutations in SCCs [50]. We found that cases with “hotspot” missense p53 mutations had higher *CSF-1* expression

than those with non-hotspot or frameshift p53 mutations (Fig. 6c). Interestingly, when we focused on cases with p53-R175H, there was a significant increase in *CSF-1* compared to cases with wild-type p53 or cases with non-hotspot missense and frameshift p53 mutations, suggesting a robust link between the p53-R175H mutation and *CSF-1* expression (Fig. 6d).

We further studied the clinical outcomes of ESCC cases in the context of tumor CSF-1 expression. In our ESCC TMA cohort, poorly differentiated ESCC had significantly higher CSF-1 expression than well-differentiated ESCC (Fig. 6e). Remarkably, stage IV tumors had higher CSF-1 expression than stage I tumors (Fig. 6f). Analysis of the TCGA ESCC dataset reinforced that the tumors in later stages (IIIa/b/c) had elevated *CSF-1* mRNA expression compared to stage Ia/b tumors (Supplementary Fig. S5b). In addition, Kaplan-Meier survival analysis of the TCGA-ESCC cohort showed that the overall survival of *CSF-1*-High ESCC cases was significantly lower (Fig. 6g), which was supported by the analyses of the correlation between CSF-1 score and probability of overall survival in the ESCC TMAs (Supplementary Fig. S5c).

We next sought to test the therapeutic efficacy of inhibiting Csf-1r *in vivo* with a neutralizing antibody (clone AFS98) for its potential to reduce lung metastasis. We injected $Trp53^{R172H/-}$ cells into athymic nude mice via tail-vein, and on Day 7 post-injection, we began treatment with either the Csf-1r neutralizing antibody or an equivalent concentration of IgG controls every other day for 8 weeks (Fig. 6h). At the pre-determined final time point (Day 56), we found that the metastatic burden in the lungs was significantly decreased in animals treated with Csf-1r neutralizing antibody (Fig. 6i).

Notably, analysis of TCGA data demonstrated a positive correlation between *CSF-1* and *CSF-1R* expression and leukocyte infiltration, with the major component being macrophages [51, 52] in ESCC cases (Supplementary Figs. S5d and S5e). Therefore, we investigated how Csf-1 might modulate the tumor microenvironment. We observed a marked increase in the migration of Raw264.7 M2 macrophages when they were cultured with $Trp53^{R172H/-}$ tumor cells compared to $Trp53^{-/-}$ or $Trp53^{+/+}$ cells (Fig. 6j). The number of migrated macrophages correlated with Csf-1 levels in conditioned media from these co-cultures: The Csf-1 concentration was approximately 350pg/mL upon co-culturing macrophages with $Trp53^{R172H/-}$ tumor cells, which was ~2- and ~20-fold higher than macrophage co-cultures with $Trp53^{-/-}$ and $Trp53^{+/+}$ cells, respectively (Fig. 6k).

To elucidate the changes in tumor-infiltrating macrophages at the metastatic site, we conducted Vectra Multiplexed Immunofluorescence in the lung tissues from Fig. 6l for total macrophages (F4/80), M2 macrophages (Cd163 and Cd206) and tumors (YFP). We observed reduced infiltration of $Cd163^{+}Cd206^{+}$ M2-polarized $F4/80^{+}$ macrophages in the YFP^{+} metastatic tumors from animals treated with the Csf-1r neutralizing antibody (Fig. 6l). These findings support the role of Csf-1/Csf-1r signaling in the crosstalk between tumor cells and macrophages, in addition to the tumor cell intrinsic properties. Overall, our findings underscore the therapeutic potential of targeting CSF-1R in metastatic ESCC in future clinical trials.

Discussion

We have demonstrated that *Trp53*^{R172H}-dependent *Csf-1* expression as an effector in mediating ESCC cell invasion and lung metastasis. Increased Csf-1 secretion in primary and metastatic tumor cells depends upon *Trp53*$^{R172H/-}$, but not wild-type p53 or the absence of p53 (p53 null). We propose that p53-R172H regulates the transcription of *Csf-1* since it interacts with the *Csf-1* promoter.

Growing evidence has demonstrated the pro-tumorigenic impact of missense p53 mutations in various cancer types [9]. In many cases, such oncogenic activities are obtained in partnership with other transcription factors and chromatin-modifying proteins [11]. In support of this notion, we discovered that Brd4, which binds to acetylated histone lysine residues [27], interacts with p53-R172H at the *Csf-1* locus and is a co-regulator in mediating the *Csf-1* transcription and promoting metastasis.

While our study demonstrates that p53-R172H binds to the promoter of *Csf-1* to induce its transcription, it is likely that other proteins might be involved in this mechanism. We identified previously that YAP/TAZ signaling is a regulator of p53-R172H-mediated lung metastasis of ESCC [34]. Interestingly, YAP1 has been reported to physically interact with BRD4 to mediate transcriptional activation, in which tumor cells depend upon transcriptional regulators to support their pro-oncogenic needs [53]. Additionally, it has been suggested that nuclear factor kappa-light-chain-enhancer of activated B cells (NF-κB) can recruit mutant p53, which in turn recruits Brd4 to active enhancers and trigger transcription of pro-inflammatory genes [54]. Thus, it is possible that NF-κB might play a role in activating p53-R172H-dependent Csf-1/Csf-1r signaling and promote lung metastasis in ESCC.

CSF-1R is expressed in epithelial cells, activating downstream pathways such as phosphatidylinositol 3-kinase (PI3K) and Ras/Raf/MAP and Src family kinases [38, 55–57]. The cell-autonomous mechanism we propose here suggests that *Trp53*$^{R172H/-}$-dependent Csf-1/Csf-1r signaling promotes the activation of Stat3 and EMT in metastatic lung lesions, and is reinforced by TCGA analysis (Figs. 3c and 3d, Supplementary Figs. 3a and 3b). Our studies suggest that loss of Csf-1 maintains cells primarily in an epithelial state. This is consistent with our previous findings on metastatic organotropism, demonstrating a selective pressure for tumor cells with low E-Cad levels to metastasize to the lungs [58].

In a recent study, Yellapu *et al.* [59] analyzed the RNA-seq data of triple-negative breast cancer (TNBC) cell lines, including MDA-MB-231, HCC-1806 and SUM-159, which were co-treated with JQ1 and the bromodomain BAZ2A/B-specific inhibitor GSK2801 to evaluate the alterations in gene expression. They identified TNF, JAK-STAT, IL-17 and NF-κB pathways as being downregulated upon co-treatment with JQ1 and GSK2801 [59]. One of the genes that was enriched in these pathways was *Vascular Endothelial Growth Factor A* (*VEGFA*) [59], which has been shown to be increased by p53-R175H and p53-R273H upon recruitment of long non-coding RNA (lncRNA) Metastasis-Associated Lung Adenocarcinoma Transcript 1 (MALAT1) in breast cancers [60]. Furthermore, *Platelet-Derived Growth Factor Receptor β* (*PDGFRβ*) was enriched in these downregulated

pathways [59], which has been demonstrated to be modulated by p53-R175H, and enhance invasion and lung metastasis in pancreatic ductal adenocarcinoma (PDAC) [61]. These pathways point to putative gene targets of mutant p53-Brd4 co-regulation that might contribute to ESCC mediated lung metastasis.

It is important to note that we do not dismiss the contribution of Csf-1/Csf-1r mediated paracrine signaling during lung metastasis. Both *in silico* TCGA analysis and our *in vivo* studies with the characterization of macrophage subpopulations upon blocking Csf-1r support the non-cell-autonomous functions of Csf-1/Csf-1r signaling. This suggests a choreographed interplay between cell autonomous and non-autonomous effects of Csf-1.

Various strategies to target p53 have been proposed, such as re-establishing wild-type p53 functions, destabilizing mutant versions of p53, inhibiting negative regulators of the wild type p53, MDM2 and MDMX to activate the tumor-suppressive function of wild-type p53, and disrupting its interaction with other proteins [9, 62]. However, most strategies to date have been ineffective. Therefore, focusing on the downstream effectors of mutant p53 has merit. We demonstrated a marked reduction in lung metastasis of $Trp53^{R172H/-}$ ESCC cells upon treatment with a neutralizing antibody targeting Csf-1r. To that end, inhibiting the CSF-1/CSF-1R signaling pathway may open up new therapeutic approaches for patients with metastatic ESCC and even other SCCs, given the high frequency of p53-R175H mutations in these SCCs [30, 50]. Treating tumor cells with a PROTAC that degrades Brd4 reduces invasion and Csf-1 secretion and treating mice with lung metastases with JQ1 decreases not only lung metastases but also Csf-1 levels in circulation. Therefore, CSF-1 may represent a possible biomarker for metastatic ESCC and help to stratify patients for CSF-1R therapy.

In summary, we propose p53-R172H/Brd4 co-regulation of *Csf-1* transcriptional expression and signaling through Csf-1r as a mechanism contributing to ESCC invasion and lung metastasis (Supplementary Fig. S6). Based on our results that are substantiated through multiple complementary genetic, pharmacological, and *in vivo* approaches, we nominate this pathway as a potential therapeutic avenue for metastatic ESCC patients who intrinsically harbor a dismal prognosis.

Methods

Cell culture

Primary and metastatic ESCC cells isolated from the mouse models were cultured in keratinocyte serum-free media supplemented with 50μg/mL bovine pituitary extract, 5ng/mL human recombinant EGF, 0.018mM $CaCl_2$, and 1% penicillin/streptomycin (KSFM; Gibco, 37010022). For drug treatments, cells were treated with 10ng/mL Csf-1r neutralizing antibody (InVivoMAb anti-mouse Csf-1r; clone AFS98; BioXCell, BE0213; RRID: AB_2687699) or IgG control (IgG2a isotype control; BioXCell, BE0089; RRID: AB_1107769) for 24 hours. To target Brd4, the cells were treated with 1μM ZXH-3–26 (MedChemExpress, HY-122826), 250 nM JQ1 (Selleckchem, S7110) or an equal volume of DMSO for 24 hours.

LS123 human colon cancer cells were cultured in Eagle's minimum essential medium (EMEM; ATCC, 30–2003; RRID: CVCL_1383) supplemented with 10% FBS and 1% penicillin/streptomycin. TE11 human ESCC cells (RRID: CVCL_TE11) were cultured in RPMI-1640 (Gibco, 11875093) supplemented with 10% fetal bovine serum (FBS) and 1% penicillin/streptomycin. All mouse and human cell lines were tested for mycoplasma frequently with MycoAlert Mycoplasma Detection Assays (Lonza, LT07–318) and the short tandem repeat (STR) profiling was conducted on human cell lines through ATCC (ATCC-135-XV).

CRISPR/Cas9 experiments

For the deletion of *Csf-1*, the ESCC cell lines were nucleofected with 2.5μg of Spyfi Cas9 (Aldevron, 9214) and two pairs of gRNAs (Synthego, Supplementary Table S1) using a ribonucleoprotein (RNP) approach. The Amaxa Lonza 4D Nucleofector X-Unit (Lonza, AAF-1003X) and P3 Primary Cell kit (V4XP-3024) protocol CB-150 was used for the nucleofections. 48-post nucleofection, the mixed population was sorted into 96-well plates as single cells and incubated for 3 weeks before the colonies were expanded and genotyped for the assessment of indels introduced. Colonies with homozygous indels were verified by qRT-PCR and ELISA.

Deletion of *TP53* in LS123 or TE11 cells was achieved by infecting pLentiCRISPR v2 (GenScript) with human *TP53* sgRNA (Supplementary Table S1) or an empty control vector. The cells were sorted 48 hours after the infection into single cell colonies in 96-well plates and treated with 1.5μg/mL or 2.0μg/mL Puromycin for 2 weeks, respectively. Viable colonies were expanded and the p53 levels were verified by immunoblotting.

Lentiviral overexpression

The *Csf-1* (Myc-DDK-tagged) cDNA (Origene, MR226827) was cloned into the pLenti-C-mRFP-P2A-Puro-Lenti vector (Origene, PS100094) at the *SgfI-MluI* restriction enzyme sites. The plasmid was amplified and verified using the forward primer 5'-GGACTTTCCAAAATGTCG-3'. The cells were infected either with 1μg of the Csf-1 overexpression plasmid or an empty control vector. After infection, the cells were treated with 2μg/mL Puromycin for two weeks. The Csf-1 expression was verified by qRT-PCR and ELISA.

shRNA and siRNA knockdown

To achieve Brd4 knockdown with shRNA, cells were transduced with pGFP-C-shLenti lentiviral particles with non-target, shBrd4 A, and shBrd4 B (Origene, TR30023; Supplementary Table S1). After 48 hours, stable colonies were selected using 2μg/mL Puromycin (Sigma Aldrich). qRT-PCR and Western blotting were performed to confirm knockdown efficiency.

For Brd4 knockdown with siRNA, Accell SMARTPool targeting mouse Brd4 (Horizon Discovery; Supplementary Table S1) was used according to the manufacturer's instructions. Briefly, the cells were treated with 1μM siBrd4 or non-target control (Horizon Discovery; Supplementary Table S1) in siRNA Delivery Media (Horizon Discovery, B-005000) and

incubated for 72 hours at 37°C with 5% CO_2. qRT-PCR and Western blotting were performed to confirm knockdown efficiency after 96 hours.

Animal studies

L2-Cre; *LSL-Trp53*$^{+/+}$, *Trp53*$^{-/-}$, or *Trp53*$^{R172H/-}$; *Rosa26*$^{lox\text{-}Stop\text{-}lox\text{-}YFP}$ mice were generated and treated with 4-NQO as described previously [32]. All animal studies were approved by Institutional Animal Care and Use Committee at Columbia University, and all experiments were conducted in compliance with the NIH guidelines for animal research.

We used lateral tail-vein injections to model lung metastasis as described previously [34]. Briefly, 1.0×10^6 dissociated single-cells were resuspended in 100μL of cold phosphate-buffered saline (PBS) and injected into the distal end of the lateral tail-vein of 7-week-old athymic nude mice (CrTac:NCr-*Foxn1*^{nu}, Taconic Bioscience; RRID: IMSR_TAC:NCRNU). Throughout the experiments, mice were monitored daily for signs of pain, discomfort and/or weight loss. To assess metastatic burden, mice were euthanized at 8 weeks by CO_2 and cervical dislocation. The lungs were harvested and flushed with 20 mL of Heparin-PBS to reduce red blood cells, imaged with Keyence BZ-X800 (Keyence) microscope, and the metastatic burden was quantified as number of YFP$^+$ metastatic foci. 200μg of Csf-1r neutralizing antibody (*InVivoMAb* anti-mouse Csf-1r; clone AFS98; BioXCell, BE0213; RRID: AB_2687699) or equivalent IgG (IgG2a isotype control; BioXCell, BE0089; RRID: AB_1107769) was injected intraperitoneally between days 7 and 53 after the initial tail-vein injections. 100mg JQ1 (Selleckchem, S7110) was dissolved in 1ml of DMSO, and then added to 19ml of 20% captisol (20% SBE-β-CD in saline) to yield 5mg/mL. 50mg/kg of JQ1 or equivalent volume of vehicle control was injected intraperitoneally every other day between days 7 and 53 after the initial tail-vein injections.

For subcutaneous injections, after anesthesia, 3.0×10^6 tumor cells were resuspended in 100μl of 1:1 cold Matrigel:PBS was injected into the right and left dorsal flanks of the athymic nude mice (CrTac:NCr-*Foxn1*^{nu}, Taconic Bioscience; RRID: IMSR_TAC:NCRNU). 1 week after the subcutaneous transplantation, tumor growth was measured every other day. At Day 28, mice were sacrificed, tumors were harvested, and their weights were measured, and harvested tumors were analyzed by histology and immunohistochemistry.

Invasion assays

The Transwell invasion assay was conducted using Corning BioCoat Matrigel™ invasion chamber (Corning, 354481). The 1.0×10^5 cells resuspended in 500μL of serum-free KSFM were seeded in the upper chamber, and 500μL of standard KSFM was added under the chamber. After 24-hour incubation at 37°C, the invading cells were fixed with 70% ethanol for 15 minutes and stained with 2% Crystal-Violet for 10 minutes at room temperature. The number of invading cells was counted using Keyence BZ-X800 (Keyence) microscope.

RNA isolation, cDNA synthesis and qRT-PCR

RNA samples were extracted using the QIAGEN Mini RNeasy kit (#74104) according to the manufacturer's instructions. cDNA from 1μg of RNA was synthesized with iScript Reverse Transcription Supermix (Bio-Rad, 1708841). qRT-PCR was performed using the

StepOnePlus real-time PCR system (Applied Biosystems) and TaqMan Universal PCR Master Mix (Applied Biosystems, 4304437) and TaqMan Gene Expression Assays with the best coverage as listed in Supplementary Table S1. Relative expression was analyzed using the comparative Ct method (ΔΔCt) and compared to PPIA, a control endogenous gene.

Immunoblotting

The immunoblotting was performed as described previously [63]. Briefly, cell pellets were resuspended in a 50–150μL of cell lysis buffer [20mM Tris–HCl [pH 7.5], 150mM NaCl, 1mM Na_2EDTA, 1mM EGTA, 1% [vol/vol] Triton X-100, 2.5mM sodium pyrophosphate, 1mM β-glycerophosphate, 1mM Na_3VO_4, and 1X complete EDTA-free protease inhibitor cocktail (Roche). Protein lysates were quantified with Bio-Rad protein assay and 0.5–2μg/μl solutions were prepared using 4X Laemmli sample buffer (Bio-Rad). 10–30μg of samples were loaded into 4–15% mini-protean TGX precast gels (Bio-Rad) and transferred to 0.2μm nitrocellulose membrane with Trans-blot turbo mini transfer packs (Bio-Rad). After blocking in 5% milk in PBS for 60 minutes, membranes were incubated with the primary antibody for 16 hours at 4ºC, followed by incubation with a secondary antibody for 60 minutes at room temperature. Antibodies were diluted in 5% bovine serum albumin in PBS + 0.1% tween20. The membranes were imaged using Chemidoc imaging system (Bio-Rad).

Immunohistochemistry and immunofluorescence staining

All the tissues were fixed in buffered zinc formalin (Thermo Fisher, 22–050-259) for 18 hours at 4°C, washed in PBS for 30 minutes and placed in 70% ethanol. Antigen retrieval was performed on dewaxed and rehydrated FFPE sections using 10mM boiling citric acid buffer (pH=6) (immunohistochemistry) or R-Buffer A (Fisher Scientific, 50311711; immunofluorescence) in a pressure cooker. For immunohistochemistry staining, endogenous peroxidases were quenched with 3% H_2O_2 (Sigma Aldrich, H1009), followed by blocking with Avidin (Sigma-Aldrich, A9275), Biotin (Sigma-Aldrich, B4501) and Starting Block T20 buffer (Thermo Fisher, 37543) for 15 each at room temperature. The tissue sections were incubated with primary antibodies (Supplementary Table S2) for approximately 16 hours at 4°C, and followed by incubation with biotinylated secondary antibodies (Vector Laboratories) for 30 minutes at 37°C (Supplementary Table S2). All antibodies were diluted in PBS+1% Bovine serum albumin+0.3% TritonX buffer. Slides were then incubated with ABC reagent (Vector Laboratories, PK-6100) for 30 minutes at 37°C, treated with DAB substrate kit (Vector Laboratories, SK4100), counterstained with Hematoxylin, dehydrated and mounted for imaging.

For immunofluorescence staining, FFPE tissue sections or cells that were fixed with 4% PFA and permeabilized with 0.1% TritonX were blocked with PBS+5% donkey serum+0.3% TritonX blocking buffer for 1 hour at room temperature. All the primary antibodies were diluted in the same blocking buffer and incubated for approximately 16 hours at 4°C, followed by incubation with Alexa Fluor antibodies for 1 hour at room temperature (Supplementary Table S2). Brightfield and fluorescent images were taken either with Keyence BZ-X800 (Keyence) or Leica AT2 whole-slide digital imaging (Leica).

Flow cytometry

For Csf-1r flow cytometry, the mouse ESCC and Raw264.7 cells were dissociated into single cells with Hank's Enzyme Free Cell Dissociation Solution (EMD Millipore, S-004-C) and filtered through a 100-μm strainer. Cells were stained with anti-Csf1r or isotype control (Supplementary Table S2) in a staining solution at 4°C for 30 minutes. Cells were washed three times in staining solution and then stained with SYTOX Red (Thermo Fisher, S34859) for flow cytometric analysis.

Multiplex immunofluorescence

On FFPE lung tissue sections, Vectra-6plex multiplex immunofluorescence was conducted with antibodies with specific Opal fluorophores directed against YFP, F4/80, Cd163 and Cd206 for metastatic tumor cells, total and M2-polarized macrophages (antibodies listed in Supplementary Table S2). The stained sections were imaged using a multispectral camera (VECTRA® Quantitative Pathology Workstation), followed by signal unmixing, segmentation and single-cell quantification using quPath analysis software (RRID: SCR_018257).

Proximity ligation assay (PLA)

PLA assays were conducted using Duolink In Situ Red Starter kit (Sigma Aldrich, DUO92101), according to the manufacturer's instructions. The primary antibodies and dilutions used are listed in (Supplementary Table S2). ImageJ software (RRID:SCR_003070) was used to quantify PLA signal per nuclei.

Cytokine array

The metastatic ESCC cells were grown in mono-culture for 48 hours and their conditioned media were collected after centrifuging for 10 minutes at 4°C and 2,000rpm. The relative concentrations of 62 cytokines were measured using the mouse cytokine array C3 (Raybiotech, AAM-CYT-3–2).

ELISA

The standard culture medium was replaced by serum-free medium 24 hours after the initial seeding of the cells. The mono- and co-cultures were incubated at 37 ºC for 48 hours, and the conditioned medium was collected by centrifugation for 10 minutes at 2,000rpm at 4ºC. Secreted Csf-1 levels were measured using the Mouse M-CSF Quantikine ELISA Kit (R&D Systems, MMC00B), according to the manufacturer's instructions. The absorbance was read at 450nm with a correction wavelength of 540nm, and the final absorbance was calculated by subtracting the 540-nm correction from the 450-nm readout.

Chromatin immunoprecipitation

3.0×10^7 primary and metastatic ESCC cells were collected and washed once in PBS and then crosslinked in 10mL of 1% Formaldehyde in PBS solution (Thermo Fisher, 28908) for 10 minutes at room temperature. The reaction was stopped by adding 0.5ml glycine at a final concentration of 125mM for 5 minutes at room temperature. Chromatin immunoprecipitation, including cell lysis, sonication, immunoprecipitation and purification

was conducted using an anti-p53 antibody (CM5, Supplementary Fig. S2) as previously described [64]. The ChIP products were quantified using the StepOnePlus real-time PCR system (Applied Biosystems) using the reaction mix with the Power SYBR Green PCR Master Mix (Applied Biosystems, 4367659) and primers as listed in the Supplementary Table S1. The values were normalized to the amount of DNA detected in the input samples by qRT-PCR.

Human ESCC and SCC specimens

We obtained well-annotated tissue microarrays (TMAs) representing surgically removed, paired primary ESCC tumors and adjacent normal mucosa from Institutional Review Board (IRB)-approved and de-identified therapy-naive patients (n=148), as described in [65, 66].

We accessed the TCGA for the analysis of survival, tumor staging, gene expression and mutation data in ESCC and SCC cases at https://gdc.cancer.gov/about-data/publications/pancanatlas. SCC tumors are listed in [30], and separates esophageal adenocarcinoma (EAC) from ESCC cases. The analysis of leukocyte infiltration is described in [51].

CUT & RUN-seq sample preparation

CUT&RUN-seq sample preparation was performed following a protocol published [67]. Briefly, 3.0×10^5 ESCC tumor cells per condition were harvested and lightly crosslinked with 0.1% Formaldehyde in PBS solution (Thermo Fisher, 28908) for 1 minute at room temperature. Cells bound to activated Biomag Plus Concavalin A beads (Bangs Laboratories, BP531) were incubated with primary antibodies for IgG or H3K27ac on nutator overnight at 4ºC (Supplementary Table S2). After binding pAG-MNase (EpiCypher, 15–1016), the targeted chromatin was digested with 100mM $CaCl_2$ for 30 minutes at 0ºC and the DNA was isolated using phenol-chloroform extraction. *E. coli* spike-in DNA (EpiCypher, 18–1401) was used for NGS normalization. The library preparation on the purified DNA was conducted with NEBNext Ultra II DNA Library Prep Kit for Illumina (BioLabs, E7103) following the manufacturer's instructions.

CUT&RUN-seq data analysis

Reads were aligned to the mouse reference genome mm10 using Bowtie v2.2.8 (RRID: SCR_005476) with parameters -q -I 50 -X 700 --very-sensitive-local --local --no-mixed --no-unal --no-discordant, and reads quality was assessed using fastQC. Statistics of aligned reads for each sample is provided in Supplementary Table S3. Binary alignment map (BAM) files were generated with samtools v1.9 (RRID: SCR_002105) and were used in downstream analysis. MACS2 v2.1.0 was used to called significant peaks. Peaks within ENCODE blacklisted regions were removed. Coverage tracks were generated from BAM files using deepTools [68], bamCoverage with parameters –binsize 1 and scaled with DEseq2 scaling factors. The BAM files were merged into a single BAM and significant peaks were called using MACS2 narrowPeak 2.1.0 to generate a bed file with the universe of regions. featureCounts from subread v2.0.1 (RRID: SCR_009803) was used to report the count of alignments from each samples BAMs at the universe of regions and generate a counts matrix. Next, the R package DEseq2 v1.34 (RRID: SCR_015687) was used to identify differentially enriched peaks and generate PCA and MA plots. Differential regions

were called if the adjusted p-value was less than 0.05. Heatmaps of genomic regions were generated with deepTools 3.2.1 (RRID: SCR_016366). The command computeMatrix was used to calculate scores at genomic regions and to generate a matrix file for use with plotHeatmap to generate plots.

Histopathologic analysis

All pathologic analyses were performed by Dr. Andres J. Klein-Szanto (Histopathology Facility, Fox Chase Cancer Center) in accordance with the consensus report and recommendations for pathologic analysis. The quantitative evaluation of positive cells (Ki67, p53, CSF-1, CSF-1R) or nuclei (Stat3), as well as the score of elongated tumor cells, was performed by counting manually 300 to 500 cells per case on every slide in a blinded fashion. For IHC analysis, 0 indicated negative staining; 1, weak staining; 2, moderate staining; and 3, strong staining. The H-score was calculated as [3×(% strong staining)]+[2×(% moderate staining)]+[1×(% weak staining)], yielding a range of 0–300.

RNA-seq analysis

STAR 2.7.10 was used to align trimmed fastq files to the reference genome (mm10), and Picard CollectRnaSeqMetrics module (Picard) was used to evaluate alignments and perform initial QC. Gene expression was quantified with HTSEQ, and this data was imported into Rstudio (R 3.5) and used as an input file for DeSeq2 (RRID: SCR_015687) analysis to determine differentially expressed genes across different conditions. Differentially expressed genes were used as input for Volcano plot and GSEA analysis.

Statistical analysis

All data are presented as the mean ± standard error mean (SEM), and sample size and replicates are indicated in the text and figure legends. Statistical significance was set at $p<0.05$. The statistical analyses, including Student unpaired t test, One-way ANOVA and Mann-Whitney U test were performed using GraphPad Prism 9.0 (GraphPad Software; RRID: SCR_002798) and the False Discovery Rate (FDR) method was used for the adjustment of p-values (p_{adj}). For the correlation analyses, Spearman correlation coefficients were used. Power analysis was conducted with our Biostatistics Shared Resources.

Supplementary Material

Refer to Web version on PubMed Central for supplementary material.

Acknowledgments

This work was funded by National Institutes of Health (NIH)/National Cancer Institute (NCI) grants P01-CA098101 (A.K.R.), P30CA013696 (A.K.R.) and R01CA272903–01 (A.K.R.), the American Cancer Society Research Professorship (A.K.R.), the NIH/NCI fellowship F31CA275369–02 (G.E.), the NIH/NCI grant R35CA220526 (C.P.) and Office of Research Infrastructure of the NIH under award number S10OD026880 (D.H. and S.C.). We thank the Confocal and Special Microscopy, Molecular Pathology, Human Immune Monitoring and Biostatistics Shared Resources at the Herbert Irving Comprehensive Cancer Center (HICCC), and Flow Cytometry Core at the Columbia Stem Cell Initiative (CSCI) of Columbia University Irving Medical Center. We also thank to Theresa Swayne (Columbia University) for technical assistance and input on confocal imaging and quantification of multiplex immunofluorescence. This work was supported in part by the Bioinformatics for Next Generation Sequencing (BiNGS) shared resource facility within the Tisch Cancer Institute at the Icahn School of Medicine at Mount Sinai, which is partially funded by the NIH/NCI grant P30CA196521. This work was also supported

in part through the computational resources and staff expertise provided by Scientific Computing at the Icahn School of Medicine at Mount Sinai and supported by the Clinical and Translational Science Awards (CTSA) grant UL1TR004419 from the National Center for Advancing Translational Sciences (NCATS).

Data availability

CUT&RUN-seq raw and processed data reported in this article have been deposited at the NCBI Gene Expression Omnibus (GEO; RRID:S CR_005012) with accession number: GSE232757 and are publicly available as the date of publication. This paper also analyzes existing, publicly available data from The Cancer Genome Atlas (TCGA) and can be accessed from The Genomic Data Common (GDC), https://gdc.cancer.gov/about-data/publications/pancanatlas. This paper does not report original code. The scripts and parameters of each step can be provided upon request to the authors.

References

1. Pachmayr E, Treese C, and Stein U, Underlying Mechanisms for Distant Metastasis - Molecular Biology. Visc Med, 2017. 33(1): p. 11–20. [PubMed: 28785563]
2. Lambert AW, Pattabiraman DR, and Weinberg RA, Emerging Biological Principles of Metastasis. Cell, 2017. 168(4): p. 670–691. [PubMed: 28187288]
3. Fares J, Fares MY, Khachfe HH, Salhab HA, and Fares Y, Molecular principles of metastasis: a hallmark of cancer revisited. Signal Transduct Target Ther, 2020. 5(1): p. 28. [PubMed: 32296047]
4. Freed-Pastor WA and Prives C, Mutant p53: one name, many proteins. Genes Dev, 2012. 26(12): p. 1268–86. [PubMed: 22713868]
5. Sabapathy K. and Lane DP, Therapeutic targeting of p53: all mutants are equal, but some mutants are more equal than others. Nat Rev Clin Oncol, 2018. 15(1): p. 13–30. [PubMed: 28948977]
6. Wang H, Guo M, Wei H, and Chen Y, Targeting p53 pathways: mechanisms, structures, and advances in therapy. Signal Transduct Target Ther, 2023. 8(1): p. 92. [PubMed: 36859359]
7. Schulz-Heddergott R, Stark N, Edmunds SJ, Li J, Conradi LC, Bohnenberger H, et al. , Therapeutic Ablation of Gain-of-Function Mutant p53 in Colorectal Cancer Inhibits Stat3-Mediated Tumor Growth and Invasion. Cancer Cell, 2018. 34(2): p. 298–314 e7. [PubMed: 30107178]
8. Stein Y, Rotter V, and Aloni-Grinstein R, Gain-of-Function Mutant p53: All the Roads Lead to Tumorigenesis. Int J Mol Sci, 2019. 20(24).
9. Tang Q, Su Z, Gu W, and Rustgi AK, Mutant p53 on the Path to Metastasis. Trends Cancer, 2020. 6(1): p. 62–73.
10. Redman-Rivera LN, Shaver TM, Jin H, Marshall CB, Schafer JM, Sheng Q, et al. , Acquisition of aneuploidy drives mutant p53-associated gain-of-function phenotypes. Nat Commun, 2021. 12(1): p. 5184. [PubMed: 34465782]
11. Kim MP and Lozano G, Mutant p53 partners in crime. Cell Death Differ, 2018. 25(1): p. 161–168. [PubMed: 29099488]
12. Muller PA and Vousden KH, Mutant p53 in cancer: new functions and therapeutic opportunities. Cancer Cell, 2014. 25(3): p. 304–17. [PubMed: 24651012]
13. Noll JE, Jeffery J, Al-Ejeh F, Kumar R, Khanna KK, Callen DF, et al. , Mutant p53 drives multinucleation and invasion through a process that is suppressed by ANKRD11. Oncogene, 2012. 31(23): p. 2836–48. [PubMed: 21986947]
14. Lv T, Lv H, Fei J, Xie Y, Lian D, Hu J, et al. , p53-R273H promotes cancer cell migration via upregulation of neuraminidase-1. J Cancer, 2020. 11(23): p. 6874–6882. [PubMed: 33123278]
15. Kadosh E, Snir-Alkalay I, Venkatachalam A, May S, Lasry A, Elyada E, et al. , The gut microbiome switches mutant p53 from tumour-suppressive to oncogenic. Nature, 2020. 586(7827): p. 133–138. [PubMed: 32728212]
16. Morgan E, Soerjomataram I, Rumgay H, Coleman HG, Thrift AP, Vignat J, et al. , The Global Landscape of Esophageal Squamous Cell Carcinoma and Esophageal Adenocarcinoma Incidence

and Mortality in 2020 and Projections to 2040: New Estimates From GLOBOCAN 2020. Gastroenterology, 2022. 163(3): p. 649–658 e2.

17. Tsai TJ, Mukundan A, Chi YS, Tsao YM, Wang YK, Chen TH, et al. , Intelligent Identification of Early Esophageal Cancer by Band-Selective Hyperspectral Imaging. Cancers (Basel), 2022. 14(17).
18. Rustgi A. and El-Serag HB, Esophageal carcinoma. N Engl J Med, 2015. 372(15): p. 1472–3.
19. Bellini MF, Cadamuro AC, Succi M, Proenca MA, and Silva AE, Alterations of the TP53 gene in gastric and esophageal carcinogenesis. J Biomed Biotechnol, 2012. 2012: p. 891961.
20. Song Y, Li L, Ou Y, Gao Z, Li E, Li X, et al. , Identification of genomic alterations in oesophageal squamous cell cancer. Nature, 2014. 509(7498): p. 91–5. [PubMed: 24670651]
21. Dwyer AR, Greenland EL, and Pixley FJ, Promotion of Tumor Invasion by Tumor-Associated Macrophages: The Role of CSF-1-Activated Phosphatidylinositol 3 Kinase and Src Family Kinase Motility Signaling. Cancers (Basel), 2017. 9(6).
22. Cannarile MA, Weisser M, Jacob W, Jegg AM, Ries CH, and Ruttinger D, Colony-stimulating factor 1 receptor (CSF1R) inhibitors in cancer therapy. J Immunother Cancer, 2017. 5(1): p. 53. [PubMed: 28716061]
23. Menke J, Kriegsmann J, Schimanski CC, Schwartz MM, Schwarting A, and Kelley VR, Autocrine CSF-1 and CSF-1 receptor coexpression promotes renal cell carcinoma growth. Cancer Res, 2012. 72(1): p. 187–200. [PubMed: 22052465]
24. Smeester BA, Slipek NJ, Pomeroy EJ, Laoharawee K, Osum SH, Larsson AT, et al. , PLX3397 treatment inhibits constitutive CSF1R-induced oncogenic ERK signaling, reduces tumor growth, and metastatic burden in osteosarcoma. Bone, 2020. 136: p. 115353.
25. Lee JE, Park YK, Park S, Jang Y, Waring N, Dey A, et al. , Brd4 binds to active enhancers to control cell identity gene induction in adipogenesis and myogenesis. Nat Commun, 2017. 8(1): p. 2217. [PubMed: 29263365]
26. Bartosovic M, Kabbe M, and Castelo-Branco G, Single-cell CUT&Tag profiles histone modifications and transcription factors in complex tissues. Nat Biotechnol, 2021. 39(7): p. 825–835. [PubMed: 33846645]
27. Donati B, Lorenzini E, and Ciarrocchi A, BRD4 and Cancer: going beyond transcriptional regulation. Mol Cancer, 2018. 17(1): p. 164. [PubMed: 30466442]
28. Hoadley KA, Yau C, Hinoue T, Wolf DM, Lazar AJ, Drill E, et al. , Cell-of-Origin Patterns Dominate the Molecular Classification of 10,000 Tumors from 33 Types of Cancer. Cell, 2018. 173(2): p. 291–304 e6. [PubMed: 29625048]
29. Song Q, Yang Y, Jiang D, Qin Z, Xu C, Wang H, et al. , Proteomic analysis reveals key differences between squamous cell carcinomas and adenocarcinomas across multiple tissues. Nat Commun, 2022. 13(1): p. 4167. [PubMed: 35851595]
30. Campbell JD, Yau C, Bowlby R, Liu Y, Brennan K, Fan H, et al. , Genomic, Pathway Network, and Immunologic Features Distinguishing Squamous Carcinomas. Cell Rep, 2018. 23(1): p. 194–212 e6. [PubMed: 29617660]
31. Li B, Cui Y, Nambiar DK, Sunwoo JB, and Li R, The Immune Subtypes and Landscape of Squamous Cell Carcinoma. Clin Cancer Res, 2019. 25(12): p. 3528–3537. [PubMed: 30833271]
32. Tang Q, Lento A, Suzuki K, Efe G, Karakasheva T, Long A, et al. , Rab11-FIP1 mediates epithelial-mesenchymal transition and invasion in esophageal cancer. EMBO Rep, 2021. 22(2): p. e48351.
33. Tang XH, Knudsen B, Bemis D, Tickoo S, and Gudas LJ, Oral cavity and esophageal carcinogenesis modeled in carcinogen-treated mice. Clin Cancer Res, 2004. 10(1 Pt 1): p. 301–13. [PubMed: 14734483]
34. Tang Q, Efe G, Chiarella AM, Leung J, Chen M, Yamazoe T, et al. , Mutant p53 regulates Survivin to foster lung metastasis. Genes Dev, 2021. 35(7–8): p. 528–541. [PubMed: 33737385]
35. Guccini I, Revandkar A, D'Ambrosio M, Colucci M, Pasquini E, Mosole S, et al. , Senescence Reprogramming by TIMP1 Deficiency Promotes Prostate Cancer Metastasis. Cancer Cell, 2021. 39(1): p. 68–82 e9. [PubMed: 33186519]

36. Li S, Qi S, Li Y, Zhang C, Sun L, Liu C, et al. , MARVELD3 inhibits the epithelial-mesenchymal transition and cell migration by suppressing the Wnt/beta-catenin signaling pathway in non-small cell lung cancer cells. Thorac Cancer, 2023. 14(12): p. 1045–1058. [PubMed: 36924014]
37. Baghdadi M, Wada H, Nakanishi S, Abe H, Han N, Putra WE, et al. , Chemotherapy-Induced IL34 Enhances Immunosuppression by Tumor-Associated Macrophages and Mediates Survival of Chemoresistant Lung Cancer Cells. Cancer Res, 2016. 76(20): p. 6030–6042. [PubMed: 27550451]
38. Giricz O, Mo Y, Dahlman KB, Cotto-Rios XM, Vardabasso C, Nguyen H, et al. , The RUNX1/IL-34/CSF-1R axis is an autocrinally regulated modulator of resistance to BRAF-V600E inhibition in melanoma. JCI Insight, 2018. 3(14).
39. Mertens B, Cristina T. Araujo Nogueira de, Topalis D, Stranska R, Snoeck R, and Andrei G, Investigation of tumor-tumor interactions in a double human cervical carcinoma xenograft model in nude mice. Oncotarget, 2018. 9(31): p. 21978–22000. [PubMed: 29774117]
40. Lin WH, Chang YW, Hong MX, Hsu TC, Lee KC, Lin C, et al. , STAT3 phosphorylation at Ser727 and Tyr705 differentially regulates the EMT-MET switch and cancer metastasis. Oncogene, 2021. 40(4): p. 791–805. [PubMed: 33262462]
41. Pradeepa MM, Causal role of histone acetylations in enhancer function. Transcription, 2017. 8(1): p. 40–47. [PubMed: 27792455]
42. Karakasheva TA, Lin EW, Tang Q, Qiao E, Waldron TJ, Soni M, et al. , IL-6 Mediates Cross-Talk between Tumor Cells and Activated Fibroblasts in the Tumor Microenvironment. Cancer Res, 2018. 78(17): p. 4957–4970. [PubMed: 29976575]
43. Lo W, Parkhurst M, Robbins PF, Tran E, Lu YC, Jia L, et al. , Immunologic Recognition of a Shared p53 Mutated Neoantigen in a Patient with Metastatic Colorectal Cancer. Cancer Immunol Res, 2019. 7(4): p. 534–543. [PubMed: 30709841]
44. Zhou S, Zhang S, Wang L, Huang S, Yuan Y, Yang J, et al. , BET protein inhibitor JQ1 downregulates chromatin accessibility and suppresses metastasis of gastric cancer via inactivating RUNX2/NID1 signaling. Oncogenesis, 2020. 9(3): p. 33. [PubMed: 32157097]
45. Nowak RP, DeAngelo SL, Buckley D, He Z, Donovan KA, An J, et al. , Plasticity in binding confers selectivity in ligand-induced protein degradation. Nat Chem Biol, 2018. 14(7): p. 706–714. [PubMed: 29892083]
46. Devaiah BN, Mu J, Akman B, Uppal S, Weissman JD, Cheng D, et al. , MYC protein stability is negatively regulated by BRD4. Proc Natl Acad Sci U S A, 2020. 117(24): p. 13457–13467. [PubMed: 32482868]
47. Nakamura Y, Umehara T, Nakano K, Jang MK, Shirouzu M, Morita S, et al. , Crystal structure of the human BRD2 bromodomain: insights into dimerization and recognition of acetylated histone H4. J Biol Chem, 2007. 282(6): p. 4193–201. [PubMed: 17148447]
48. Wang LF, Wang Y, Yang ZY, Zhao J, Sun HB, and Wu SL, Revealing binding selectivity of inhibitors toward bromodomain-containing proteins 2 and 4 using multiple short molecular dynamics simulations and free energy analyses. SAR QSAR Environ Res, 2020. 31(5): p. 373–398. [PubMed: 32496901]
49. Rivlin N, Brosh R, Oren M, and Rotter V, Mutations in the p53 Tumor Suppressor Gene: Important Milestones at the Various Steps of Tumorigenesis. Genes Cancer, 2011. 2(4): p. 466–74. [PubMed: 21779514]
50. Dotto GP and Rustgi AK, Squamous Cell Cancers: A Unified Perspective on Biology and Genetics. Cancer Cell, 2016. 29(5): p. 622–637. [PubMed: 27165741]
51. Thorsson V, Gibbs DL, Brown SD, Wolf D, Bortone DS, Ou Yang TH, et al. , The Immune Landscape of Cancer. Immunity, 2019. 51(2): p. 411–412. [PubMed: 31433971]
52. Fang L, Hodge J, Saaoud F, Wang J, Iwanowycz S, Wang Y, et al. , Transcriptional factor EB regulates macrophage polarization in the tumor microenvironment. Oncoimmunology, 2017. 6(5): p. e1312042.
53. Zanconato F, Battilana G, Forcato M, Filippi L, Azzolin L, Manfrin A, et al. , Transcriptional addiction in cancer cells is mediated by YAP/TAZ through BRD4. Nat Med, 2018. 24(10): p. 1599–1610. [PubMed: 30224758]

54. Rahnamoun H, Lee J, Sun Z, Lu H, Ramsey KM, Komives EA, et al. , RNAs interact with BRD4 to promote enhanced chromatin engagement and transcription activation. Nat Struct Mol Biol, 2018. 25(8): p. 687–697. [PubMed: 30076409]
55. Achkova D. and Maher J, Role of the colony-stimulating factor (CSF)/CSF-1 receptor axis in cancer. Biochem Soc Trans, 2016. 44(2): p. 333–41. [PubMed: 27068937]
56. Cioce M, Canino C, Goparaju C, Yang H, Carbone M, and Pass HI, Autocrine CSF-1R signaling drives mesothelioma chemoresistance via AKT activation. Cell Death Dis, 2014. 5(4): p. e1167. [PubMed: 24722292]
57. Patsialou A, Wang Y, Pignatelli J, Chen X, Entenberg D, Oktay M, et al. , Autocrine CSF1R signaling mediates switching between invasion and proliferation downstream of TGFbeta in claudin-low breast tumor cells. Oncogene, 2015. 34(21): p. 2721–31. [PubMed: 25088194]
58. Reichert M, Bakir B, Moreira L, Pitarresi JR, Feldmann K, Simon L, et al. , Regulation of Epithelial Plasticity Determines Metastatic Organotropism in Pancreatic Cancer. Dev Cell, 2018. 45(6): p. 696–711 e8. [PubMed: 29920275]
59. Yellapu NK, Ly T, Sardiu ME, Pei D, Welch DR, Thompson JA, et al. , Synergistic anti-proliferative activity of JQ1 and GSK2801 in triple-negative breast cancer. BMC Cancer, 2022. 22(1): p. 627. [PubMed: 35672711]
60. Pruszko M, Milano E, Forcato M, Donzelli S, Ganci F, Di Agostino S, et al. , The mutant p53-ID4 complex controls VEGFA isoforms by recruiting lncRNA MALAT1. EMBO Rep, 2017. 18(8): p. 1331–1351. [PubMed: 28652379]
61. Weissmueller S, Manchado E, Saborowski M, Morris J.P.t., Wagenblast E, Davis CA, et al. , Mutant p53 drives pancreatic cancer metastasis through cell-autonomous PDGF receptor beta signaling. Cell, 2014. 157(2): p. 382–394. [PubMed: 24725405]
62. Hu J, Cao J, Topatana W, Juengpanich S, Li S, Zhang B, et al. , Targeting mutant p53 for cancer therapy: direct and indirect strategies. J Hematol Oncol, 2021. 14(1): p. 157. [PubMed: 34583722]
63. Dunbar KJ, Karakasheva TA, Tang Q, Efe G, Lin EW, Harris M, et al. , Tumor-Derived CCL5 Recruits Cancer-Associated Fibroblasts and Promotes Tumor Cell Proliferation in Esophageal Squamous Cell Carcinoma. Mol Cancer Res, 2023. 21(7): p. 741–752. [PubMed: 37027010]
64. Schmidt D, Wilson MD, Spyrou C, Brown GD, Hadfield J, and Odom DT, ChIP-seq: using high-throughput sequencing to discover protein-DNA interactions. Methods, 2009. 48(3): p. 240–8. [PubMed: 19275939]
65. Liu K, Jiang M, Lu Y, Chen H, Sun J, Wu S, et al. , Sox2 cooperates with inflammation-mediated Stat3 activation in the malignant transformation of foregut basal progenitor cells. Cell Stem Cell, 2013. 12(3): p. 304–15. [PubMed: 23472872]
66. Natsuizaka M, Whelan KA, Kagawa S, Tanaka K, Giroux V, Chandramouleeswaran PM, et al. , Interplay between Notch1 and Notch3 promotes EMT and tumor initiation in squamous cell carcinoma. Nat Commun, 2017. 8(1): p. 1758. [PubMed: 29170450]
67. Skene PJ, Henikoff JG, and Henikoff S, Targeted in situ genome-wide profiling with high efficiency for low cell numbers. Nat Protoc, 2018. 13(5): p. 1006–1019. [PubMed: 29651053]
68. Ramirez F, Ryan DP, Gruning B, Bhardwaj V, Kilpert F, Richter AS, et al. , deepTools2: a next generation web server for deep-sequencing data analysis. Nucleic Acids Res, 2016. 44(W1): p. W160–5. [PubMed: 27079975]

Significance

The invasion-metastasis cascade is a recalcitrant barrier to effective cancer therapy. We establish that the p53-R172H-dependent Brd4-Csf-1 axis is a mediator of pro-metastatic properties, correlates with patient survival and tumor stages, and its inhibition significantly reduces tumor cell invasion and lung metastasis. This axis can be exploited for therapeutic advantage.

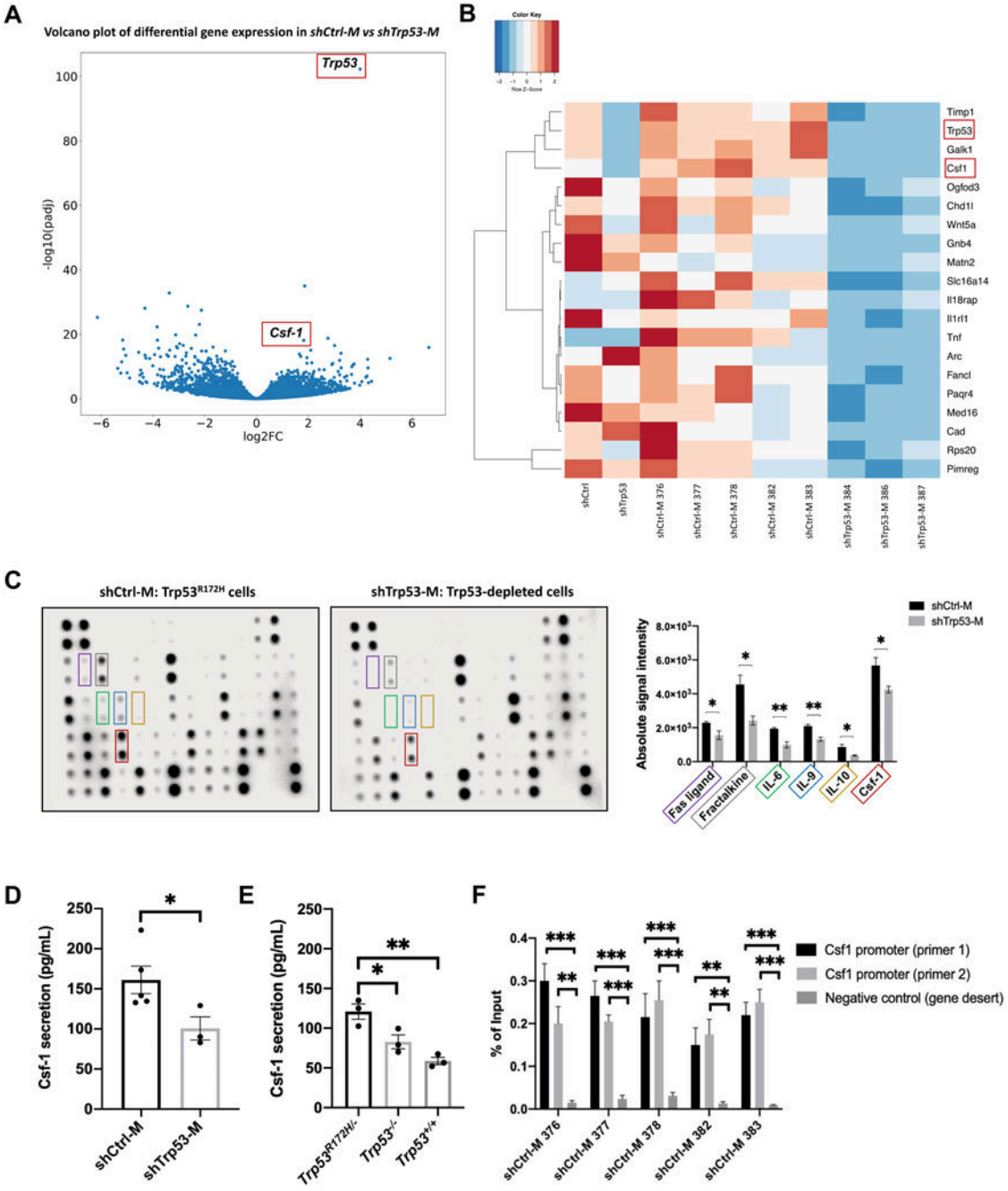

Figure 1. Colony stimulating factor-1 (Csf-1) is upregulated in a *Trp53*$^{R172H/-}$-dependent manner in ESCC lung metastasis.

(A) Volcano plot of differentially expressed genes (260 upregulated and 291 downregulated genes, P_{adj}<0.05 and |$\log_2$ fold change|>2) profiled by RNA-seq comparing shCtrl-M (n=5) with shTrp53-M (n=3). **(B)** Heatmap of the top 20 upregulated genes in primary (shCtrl vs. shTrp53) and metastatic (shCtrl-M (n=5) vs. shTrp53-M (n=3)) ESCC tumor cells (P_{adj}<0.05 and |$\log_2$ fold change|>2) based upon the comparison of shCtrl-M to shTrp53-M metastatic cells. **(C)** Representative blots of cytokine arrays with quantification of

significantly secreted factors in shCtrl-M compared to shTrp53-M metastatic cells. Csf-1 is highlighted in the red boxes, (n=3). Student unpaired t test, **p<0.01, *p<0.05. Each color-coded rectangle corresponds to the labeled cytokine from the graph. **(D)** Secreted Csf-1 levels (pg/mL) from metastatic shCtrl-M and shTrp53-M cells measured by ELISA, (n=3). Student unpaired t test, *p<0.05. **(E)** Csf-1 level (pg/mL) secreted by *Trp53*$^{R172H/-}$, *Trp53*$^{-/-}$ and *Trp53*$^{+/+}$ primary tumor cells measured by ELISA, (n=3). Student unpaired t test, **p<0.01, *p<0.05. **(F)** ChIP-qPCR for p53 occupancy at the *Csf-1* promoter in metastatic *Trp53*$^{R172H/-}$ tumor cell lines (376, 377, 378, 382 and 383) as quantified by % of Input. Experiments represent mean ± SEM in at least 3 independent replicates.

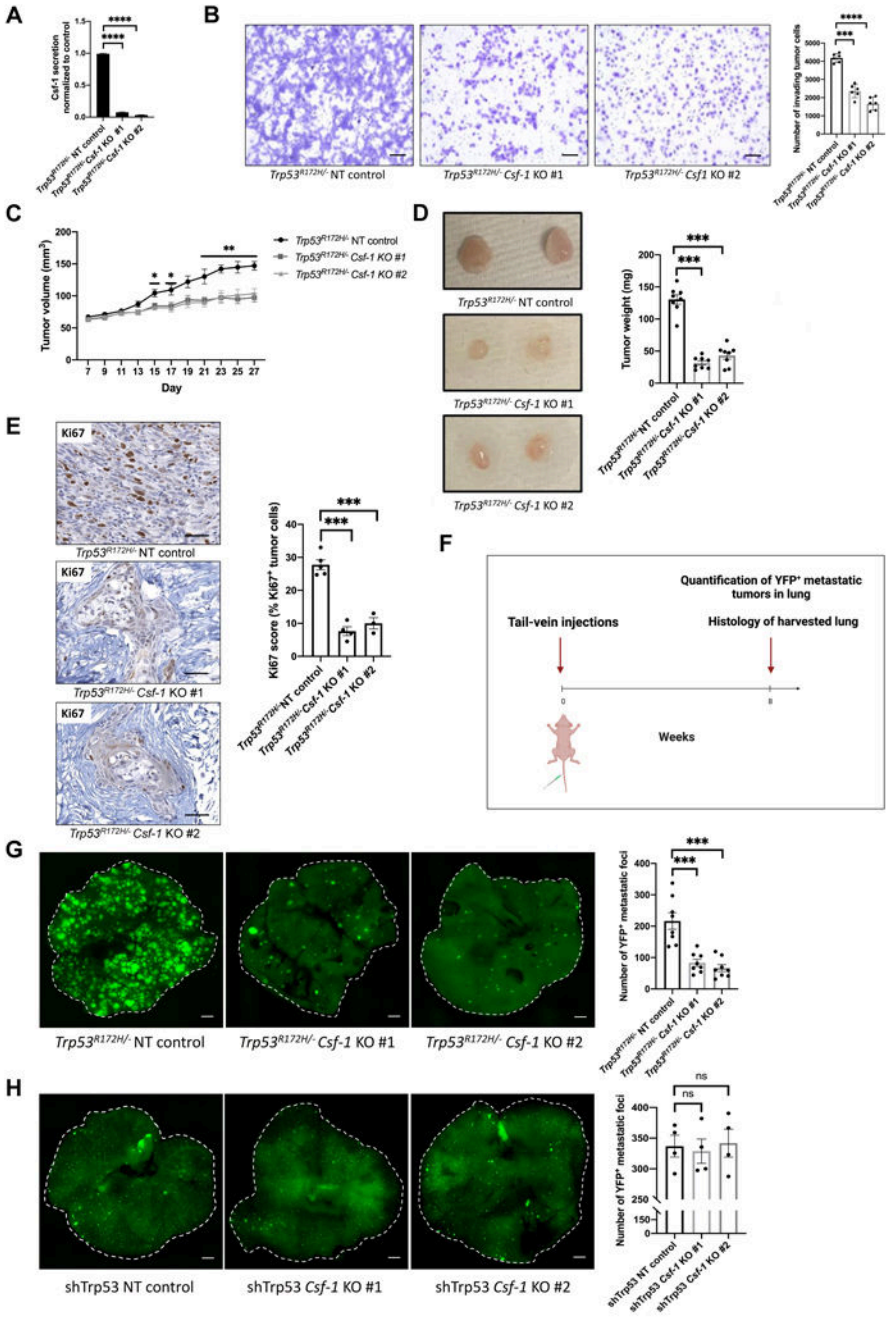

Figure 2. *Trp53*$^{R172H/-}$-dependent Csf-1 fosters cell invasion and lung metastasis.

(A) Csf-1 secretion by *Trp53*$^{R172H/-}$ Csf-1 KO #1 and KO #2 cells normalized to NT control as measured by ELISA, (n=3). Student unpaired t test, ****p<0.0001. **(B)** Representative images and quantification of invading NT and Csf-1 KO tumor cells in a Boyden chamber assay fixed and stained with Crystal Violet after 24-hour incubation, (n=3). Student unpaired t test, ****p<0.0001, ***p<0.001. Scale bar=100μm. **(C)** Volume of subcutaneous tumors (mm^3) of the implanted NT and Csf-1 KO tumor cells that is measured every other day between Day 7 and Day 27, n=5 mice, double-flank implantation (n=10/group). One-way

ANOVA, **p<0.01, *p<0.05. **(D)** Representative images and weight (mg) of subcutaneous tumors as described in (C), harvested at the end timepoint Day 28, n=5 mice, double-flank implantation (n=10/group). Student unpaired t test, ****p<0.0001, ***p<0.001. **(E)** Representative images of Ki67 immunohistochemistry and Ki67 score as quantified by the percentage of $KI67^+$ subcutaneous tumor cells at Day 28, (n=5/group). Student unpaired t test, ***p<0.001. Scale bar=50μm. **(F)** Schematic of the study of lung metastasis via tail-vein injection of tumor cells, (n=8 mice/group). **(G)** Representative images and quantification of YFP^+ metastatic foci in lung tissues harvested at Week 8, (n=8 mice/group). Student unpaired t test, ***p<0.001. **(H)** Representative images and quantification of YFP^+ metastatic foci formed after tail-vein injections of *shTrp53* NT control or Csf-1 KO cells, (n=4 mice/group). Student unpaired t test, ns: not significant. Scale bar=1mm. Experiments represent mean ± SEM in at least 3 independent replicates.

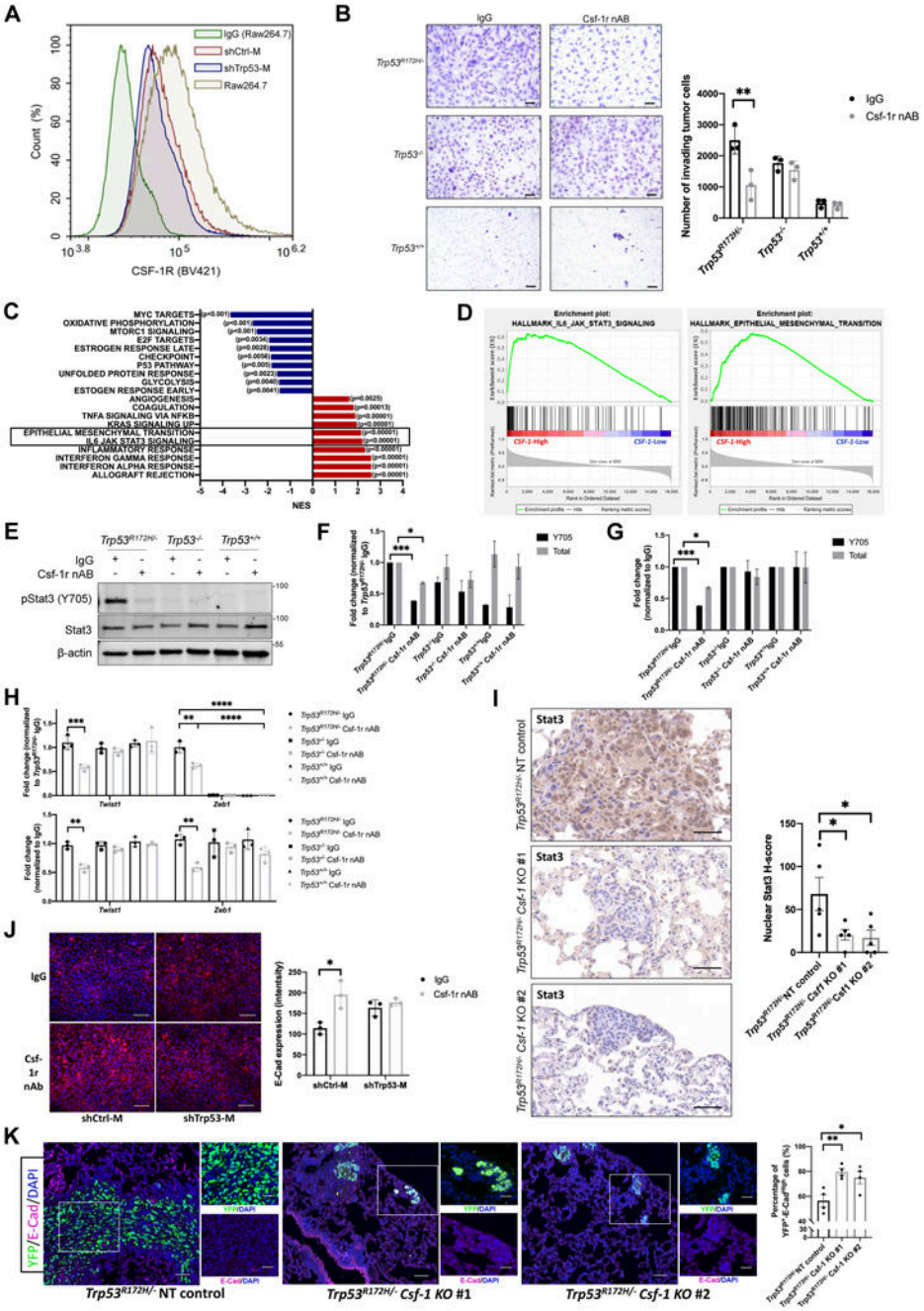

Figure 3. *Trp53*$^{R172H/-}$-dependent Csf-1 activates autocrine signaling through its cognate receptor Csf-1r to induce Stat3 activation and EMT during metastasis.

(A) Flow cytometry of Csf-1r expression in metastatic shCtrl-M and shTrp53-M ESCC cells. Murine Raw264.7 macrophages stained with the same Csf-1r antibody in BV421 and with IgG were used as positive and negative controls, respectively, (n=2). **(B)** Representative images and quantification of invading tumor cells in a Boyden chamber assay stained with Crystal Violet after 24-hour treatment with 10μg/mL of IgG or a neutralizing antibody (nAB) against Csf-1r, (n=4). Student unpaired t test, **p<0.01. Scale bar=100μm. **(C)** GSEA

plots by normalized enrichment score (NES) of pathways that correlate significantly with *CSF-1* mRNA expression based upon correlation coefficients of genes with *CSF-1* in TCGA SCC cases including lung SCC, head and neck SCC, esophageal SCC, cervical SCC and a subset of bladder cancers classified as basal squamous (red: enriched with high *CSF-1* expression, blue: enriched with low *CSF-1* expression; nominal *P* values are indicated, n=1210). **(D)** Enrichment plots for IL6-JAK-STAT3 and EMT gene sets in correlation with *CSF-1* mRNA expression in TCGA SCC cases, (n=1210). **(E)** Representative Western blots for total and phosphorylated Stat3 (Y705) in $Trp53^{R172H/-}$, $Trp53^{-/-}$ and $Trp53^{+/+}$ cells after treatment with 10μg/mL Csf-1r neutralizing antibody or IgG control for 24 hours. Beta-actin (β-actin) was used as the loading control. **(F-G)** Densitometry analysis of the Western blots in (E), normalized to the IgG treated $Trp53^{R172H/-}$ tumor cells **(F)** or normalized to IgG treated $Trp53^{R172H/-}$, $Trp53^{-/-}$ or $Trp53^{+/+}$ tumor cells **(G)**, (n=4). One-way ANOVA, ***p<0.001, *p<0.05. **(H)** Expression fold changes of *Twist1* and *Zeb1* in $Trp53^{R172H/-}$, $Trp53^{-/-}$ and $Trp53^{+/+}$ cells after treatment with 10μg/mL Csf-1r neutralizing antibody for 24 hours normalized to IgG-treated isogenic cells or IgG treated $Trp53^{R172H/-}$ cells, (n=3). One-way ANOVA, ****p<0.0001, ***p<0.001, **p<0.01. **(I)** Representative images and H-score of nuclear Stat3 levels in lung metastatic lesions with $Trp53^{R172H/-}$ NT or Csf-1 KO (Week 8), (n=5/group). Student unpaired t test, *p<0.05. Scale bar=50μm. **(J)** Representative immunocytochemistry images and scoring of E-Cad intensity of shCtrl-M and sh-Trp53-M cells after treatment with 10μg/mL Csf-1r neutralizing antibody or IgG control for 24 hours, (n=3; at least 1,000 cells). Student unpaired t test, *p<0.05. Scale bar=50μm. **(K)** Representative images and quantification of $E\text{-}Cad^{High}$ percentage in $Trp53^{R172H/-}$ NT or Csf-1 KO lung metastatic lesions (at least 5,000 YFP^{+} cells; Week 8; n=5/group). Student unpaired t test, **p<0.01, *p<0.05. Scale bar=100μm. Experiments represent mean ± SEM.

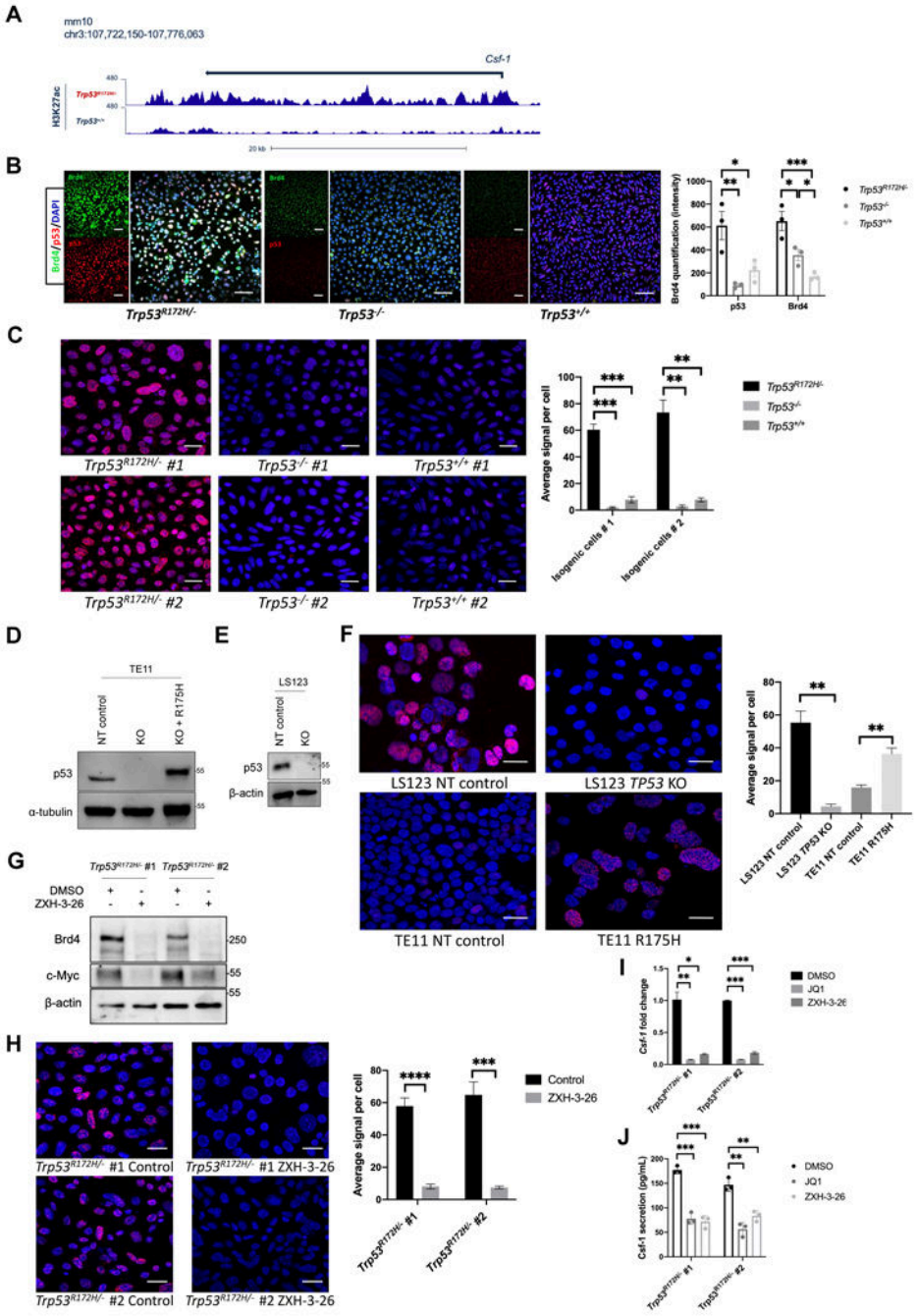

Figure 4. Brd4 is a co-regulator with p53-R172H in the induction of *Csf-1* transcription.

(A) Snapshots of the UCSC genome browser (mm10) showing the H3K27ac enrichment at the *Csf-1* locus in $Trp53^{R172H/-}$ and $Trp53^{+/+}$ cells through CUT&RUN-seq, y axis=normalized counts. **(B)** Representative confocal images of p53 (red) and Brd4 (green) immunofluorescence staining, and quantification of their intensity in $Trp53^{R172H/-}$, $Trp53^{-/-}$ and $Trp53^{+/+}$ cells. Nuclei were stained with DAPI (blue). (n=2). One-way ANOVA, ***p<0.001, **p<0.01, *p<0.05. Scale bar=50μm. **(C)** Representative confocal images of proximity ligation assay (PLA) for Brd4 and p53 and quantification of the average number

of PLA signals (red) in *Trp53*$^{R172H/-}$, *Trp53*$^{-/-}$ and *Trp53*$^{+/+}$ cells, n>100 cells (DAPI)/group, (n=4). Student unpaired t test, ****p<0.0001. Scale bar=50μm. **(D)** Representative Western blots for p53 and the loading control Alpha-tubulin (α-tubulin) in TE11 human ESCC cell lines with NT control (R110L), *TP53* KO and p53-R175H. **(E)** Representative Western blots for p53 and the loading control β-actin in LS123 NT control (R175H) and *TP53* KO. **(F)** Representative confocal images of PLA for BRD4 and p53 and quantification of the average number of PLA signals (red) in LS123 NT control, LS123 *TP53* KO, TE11 NT control, and TE11 p53-R175H, n>100 cells (DAPI)/group, (n=3). Student unpaired t test, **p<0.01. Scale bar=50μm. **(G-H)** Representative Western blots for Brd4, c-Myc and the loading control β-actin **(G),** and representative confocal images of PLA for Brd4 and p53 and quantification of the average number of PLA signals (red) **(H)** in mouse *Trp53*$^{R172H/-}$ ESCC cell lines upon 1μm ZXH-3–26 or DMSO treatment for 24 hours, n>100 cells (DAPI)/group, (n=2). Student unpaired t test, ****p<0.0001, ***p<0.001. Scale bar=50μm. **(I-J)** Csf-1 expression **(I)**, and Csf-1 secretion levels (pg/mL) **(J)** in mouse *Trp53*$^{R172H/-}$ ESCC cell lines upon 250nM JQ1, 1μM ZXH-3–26 or DMSO treatment for 24 hours, (n=3). Student unpaired t test, ***p<0.001, **p<0.01, *p<0.05. Experiments represent mean ± SEM.

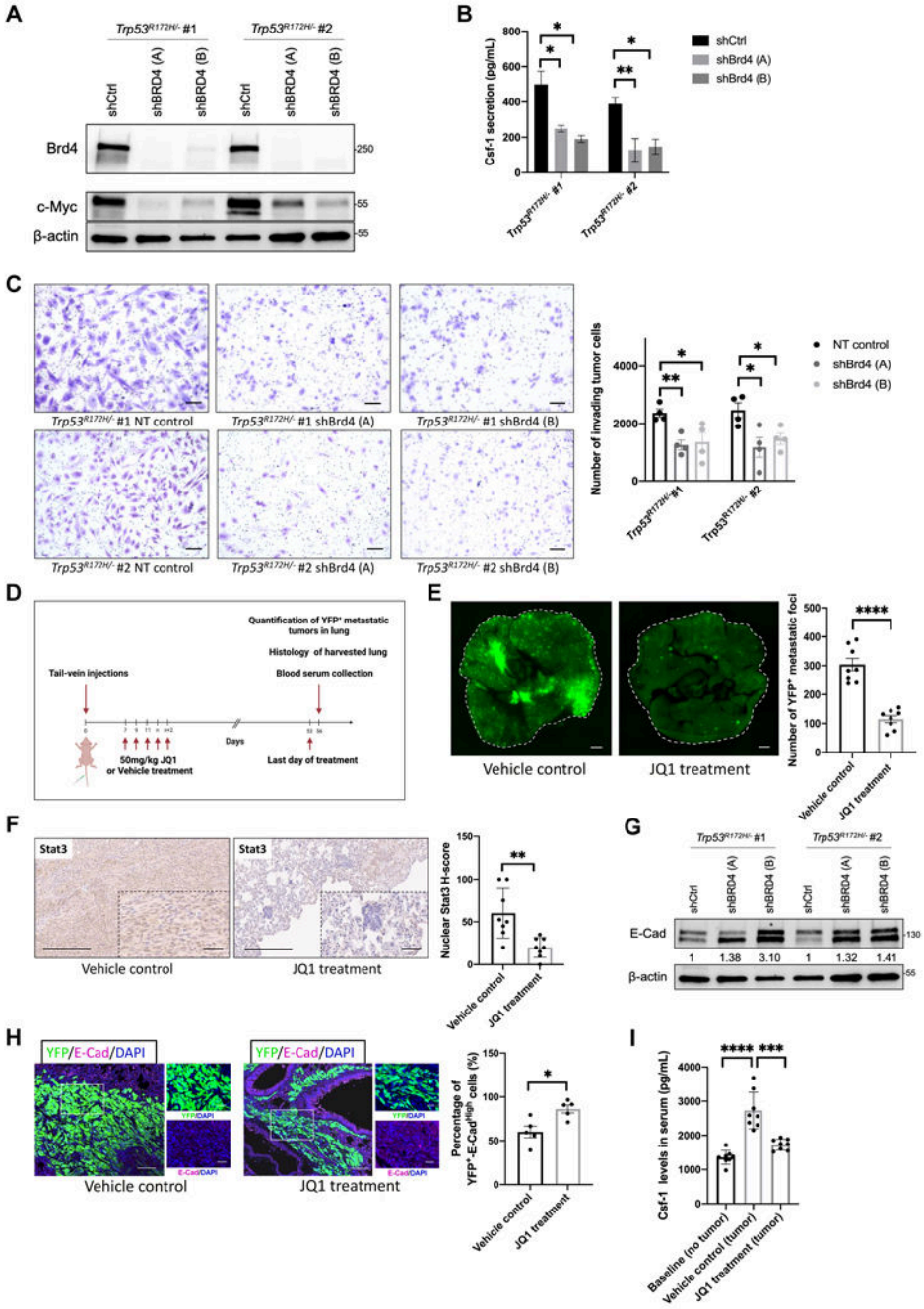

Figure 5. Brd4 contributes to ESCC tumor cell invasion and lung metastasis.

(A) Representative Western blots for Brd4, c-Myc and the loading control β-actin in mouse *Trp53*$^{R172H/-}$ ESCC cells with NT control or shBrd4A/B and densitometry analysis of Brd4 normalized to respective control in each cell line. **(B)** Csf-1 secretion levels (pg/mL) of mouse *Trp53*$^{R172H/-}$ ESCC cells with NT control or shBrd4A/B, (n=3). Student unpaired t test, **p<0.01, *p<0.05. **(C)** Representative images and quantification of invading *Trp53*$^{R172H/-}$ NT control and shBrd4A/B tumor cells fixed and stained with Crystal Violet after 24-hour incubation, (n=3). Student unpaired t test, **p<0.01,

*p<0.05. Scale bar=100μm. **(D)** Schematic of the lung metastasis experiment with JQ1 treatment after tail-vein injections of *Trp53*$^{R172H/-}$ tumor cells, (n=8 mice/group). **(E-F)** Representative images and quantification of YFP^{+} metastatic foci in lung tissues **(E)**, representative images and H-score of nuclear Stat3 from immunohistochemistry **(F)** upon vehicle control or JQ1 treatment harvested at Week 8, (n=8 mice/group). Student unpaired t test, ****p<0.0001, **p<0.01. Scale bar=1mm (E) or 300μm (lower magnification) or 60μm (higher magnification) (F). **(G)** Representative Western blot images for E-Cad, and the loading control β-actin in *Trp53*$^{R172H/-}$ NT control or shBrd4A/B ESCC cells and densitometry values normalized to respective NT control. **(H)** Representative images and quantification of E-Cad^{High} percentage in *Trp53*$^{R172H/-}$ metastatic lesions (at least 5,000 YFP^{+} cells) upon vehicle control or JQ1 treatment (Week 8), (n=5). Student unpaired t test, *p<0.05. Scale bar=100μm. **(I)** Csf-1 levels (pg/mL) in the blood sera of mice with no tumor (baseline) or with lung metastases and treated with vehicle control or JQ1 as in (D), (n=8 mice/group). One-way ANOVA, ****p<0.0001, ***p<0.001. Experiments represent mean ± SEM in at least 3 independent replicates.

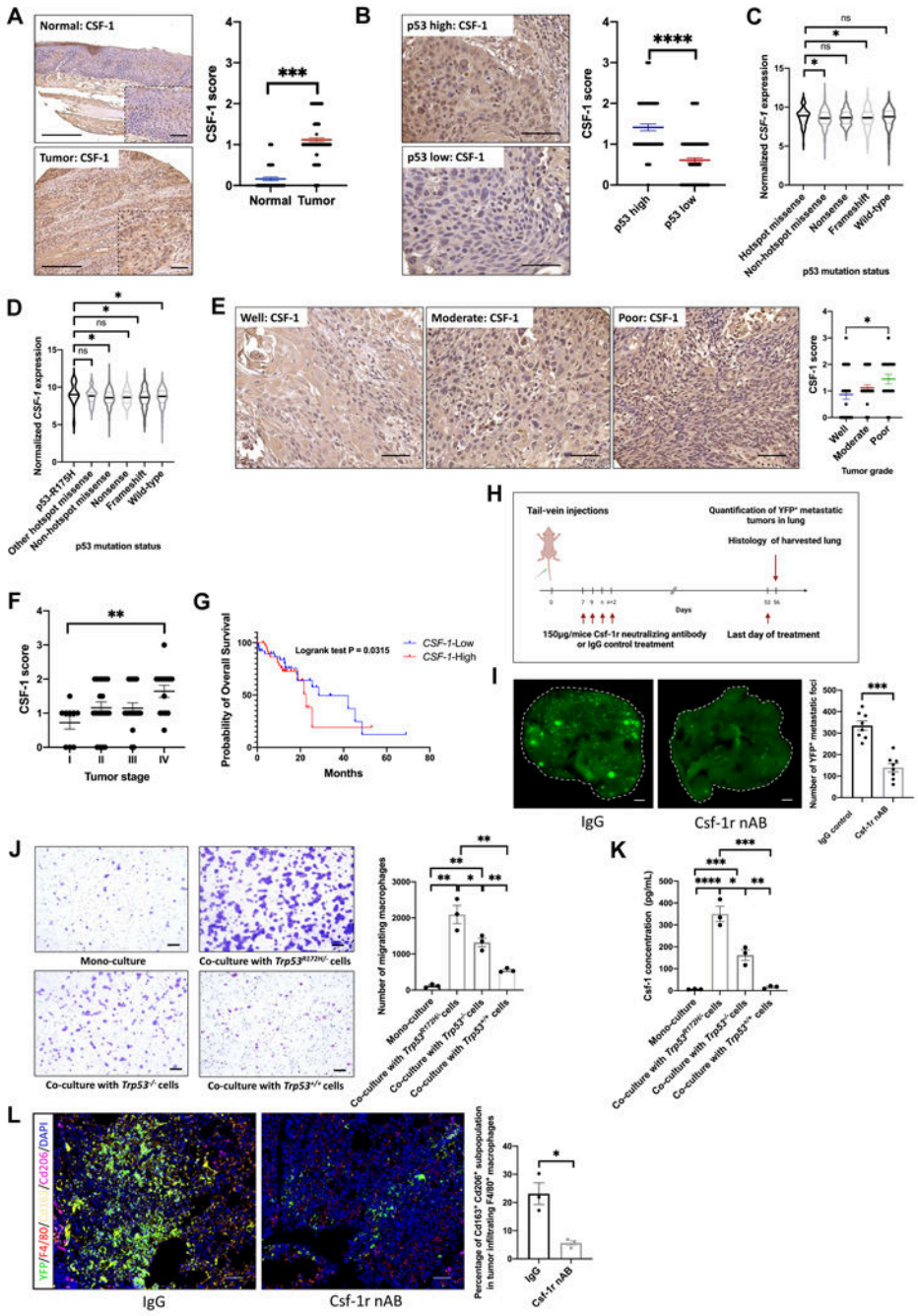

Figure 6. CSF-1/CSF-1R signaling as a potential therapeutic target.

(A) Representative images and scoring of CSF-1 expression in normal (n=47) and tumor (n=148) in ESCC tissue microarrays (TMAs), Student unpaired t test, ***p<0.001. Scale bar=300µm (lower magnification) or 60µm (higher magnification). **(B)** Representative images and scoring of CSF-1 and p53 expression in ESCC TMAs, (n=148). Student unpaired t test, ****p<0.0001. Scale bar=60µm. **(C-D)** Analysis of *CSF-1* mRNA expression in TCGA SCC samples (lung SCC, head and neck SCC, esophageal SCC, cervical SCC and a subset of bladder cancer classified as basal squamous) comparing

those having “hotspot” missense p53 mutations **(C)** or R175H **(D)** to those having “non-hotspot” or non-R175H missense, nonsense or frameshift p53 mutations or wild-type p53, (n=1210). One-way ANOVA, p-values are indicated in the graphs. **(E)** Representative images and scoring of CSF-1 in well-, moderately and poorly differentiated tumors in ESCC TMAs, (n=148). Student unpaired t test, *p<0.05. Scale bar=100μm. **(F)** CSF-1 score and correlation with ESCC tumor stages in ESCC TMAs, (n=148). One-way ANOVA, **p<0.01. **(G)** Kaplan-Meier overall survival stratified by low *CSF-1* (blue) and high *CSF-1* (red) mRNA expression in TCGA ESCC cases, (n=159), log-rank p=0.0315. **(H)** Schematic of the experiment of Csf-1r neutralizing antibody treatment of mice injected with $Trp53^{R172H/-}$ cells via tail-vein, (n=8 mice/group). **(I)** Representative images and quantification of YFP^{+} metastatic foci in lung tissues from mice upon treatment as in (H) harvested at Week 8, (n=8 mice/group). Student unpaired t test, ***p<0.001. Scale bar=1mm. **(J-K)** Representative images and quantification of migrating mouse Raw264.7 M2-macrophages **(J)**, and Csf-1 levels (pg/mL) in conditioned media **(K)** upon Raw264.7 mono-cultures or co-cultures with $Trp53^{R172H/-}$, $Trp53^{-/-}$ and $Trp53^{+/+}$ cells, (n=3). Student unpaired t test, ****p<0.0001, ***p<0.001, **p<0.01, *p<0.05. Scale bar=100μm. **(L)** Representative images of multiplex IF for YFP (green), F4/80 (red), Cd163 (yellow), Cd206 (magenta) and DAPI (blue), and quantification of % $Cd163^{+}Cd206^{+}$ tumor-infiltrating $F4/80^{+}$ macrophages in lung tissues from (K) (n=4/group). Student unpaired t test, *p<0.05. Scale bar=100μm. Experiments represent mean ± SEM and indicated in blue, red or green (A, B and E).